Interplay between Local Structure and Nuclear Dynamics in Tungstic Acid: A Neutron Scattering Study

Erwin Lalik, Kacper Drużbicki, Gavin Irvine, Matthias Gutmann, Svemir Rudić, Pascal Manuel, Václav Petříček, and Matthew Krzystyniak

Interplay Between Local Structure and Nuclear Dynamics in Tungstic Acid: a Neutron Scattering Study

Erwin Lalik,[†] Kacper Drużbicki,[‡,¶] Gavin Irvine,[§] Matthias Gutmann,[∥] Svemir Rudić,[∥] Pascal Manuel,[∥] Václav Petříček,[⊥] and Matthew Krzystyniak[*,∥]

[†]Jerzy Haber Institute of Catalysis and Surface Chemistry, Polish Academy of Sciences, Niezapominajek 8, 30-239 Cracow, Poland

[‡]Materials Physics Center, CSIC-UPV/EHU, Paseo Manuel Lardizábal 5, 20018 Donostia-San Sebastian, Spain

[¶]Centre of Molecular and Macromolecular Studies, Polish Academy of Sciences, Sienkiewicza 112, 90-363 Lodz, Poland

[§]School of Chemistry, University of St Andrews, St Andrews, Fife KY16 9ST, United Kingdom

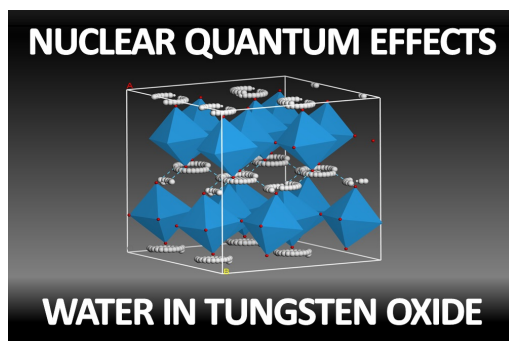[∥]ISIS Facility, Rutherford Appleton Laboratory, Chilton, Didcot, OX11 0QX, United Kingdom

[⊥]Institute of Physics, Czech Academy of Sciences, Na Slovance 1999/2, Praha 8, 182 21, Czech Republic

E-mail: matthew.krzystyniak@stfc.ac.uk*

1

Abstract

We provide an exhaustive characterization of structural properties and nuclear dynamics in tungstic acid ($WO_3 \cdot H_2O$). To this end, we employ Neutron and X-ray Diffraction (ND and XRD) combined with Inelastic Neutron Scattering (INS) and Neutron Compton Scattering (NCS) experiments, and corroborate the analysis with extensive *ab initio* modelling. The first step in our analysis is the elucidation of the crystal structure based on the refinement of low-temperature powder ND data, extending the knowledge gained from XRD analysis of a mineral specimen of tungstite. These results are confronted with low-temperature INS experiments and zero-temperature phonon calculations. The analysis reveals an inconsistency in the definition of the structure of confined water with respect to crystallographic data, also showing a concomitant fail of the phonon calculations due to a strongly anharmonic confining potential. Extending the computational route toward *ab initio* MD (AIMD) simulations allows us to probe different structural configurations and provides an improved description of the vibrational dynamics as compared to high-resolution INS experiments, nevertheless, requiring the use of effective classical temperatures. The analysis of both INS and the NCS data reveals a remarkable similarity to the nuclear dynamics earlier reported for water confined in Single-Wall Carbon Nanotubes (SWNT), which has been qualitatively described as a new phase of ice. Our analysis reveals a strong two-dimensional hydrogen-bonding network, similar to the shell model for water in SWNT. The reported NCS data show narrowing of the hydrogen momentum distribution with respect to the reference *ab initio* calculations, indicating a great deal of conformational freedom due to spatial delocalisation of protons in the ground state of the system, a clear signature of the quantum character of the nuclei.

TOC Graphic

1. Introduction

Confined interlayer water in hydrated tungsten oxides, $WO_3 \cdot nH_2O$ ($n = 1, 2$), has recently received a lot of attention.[1–4] WO_3, can crystallise into hierarchical nanostructured hydrous hexagonal WO_3 (h-WO3), a metastable hexagonal nano-structure self-assembled from h-WO3 nanorods that contain tunnels filled with water molecules and exhibits mixed electronic and ionic conductance.[1] The presence of structural water was found to lead to a transition in the energy storage mechanism from solid-state diffusion-limited in WO_3 to surface-limited (or pseudocapacitive) in $WO_3 \cdot 2H_2O$[2] and minimised the electrochemically driven deformation of the latter.[3] Concurrent electrochemical characterisation and fundamental studies of the structure and dynamics of both the solid-state structure and confined water network in $WO_3 \cdot nH_2O$ ($n = 1, 2$) have revealed that structural water is highly confined and most probably stabilises the layered structure as it undergoes intercalation-induced phase transformations at high rates.[4] Concretely, the QuasiElastic Neutron Scattering (QENS) and solid-state Nuclear Magnetic Resonance (ss-NMR) investigations revealed the presence of only localised and not the translational motion of water molecules up to the nanosecond time scales.

Water, especially in the confined state, has been the driving force of the research on Nuclear Quantum Effects (NQEs) in condensed matter systems.[5,6] It is largely owing to the investigation of NQEs in water and their relation to water properties[7–18] that the experimental techniques such as neutron Compton scattering (NCS), also termed as Deep Inelastic Neutron Scattering (DINS),[5,6,19–26] have risen to prominence. According to these and other investigations, water in confined spaces forms otherwise inaccessible liquid and glassy phases that exist over a wide range of temperatures, where protons in the hydrogen bonds (H-bonds) are coherently delocalised and may exhibit nuclear quantum tunnelling.[7–10,14–16] These highly unusual states of water lead to the observation of anomalous effects such as a deficit of nuclear kinetic energy[10,18] and unusual transport properties.[10]

The joint effort on both experimental and theoretical fronts led to a paradigm change in

modern investigation of materials exhibiting NQEs by means of neutrons, whereby tradition-ally employed techniques such as Neutron Diffraction (ND) and Inelastic Neutron Scattering (INS) were complemented with NCS and augmented with increasingly more sophisticated *ab initio* modelling protocols.[8,10,12,14,27–41] In such a way, the peculiarities of the local structure and dynamics, dictating important material properties that would otherwise have escaped the experimental scrutiny of ND, could be captured by the INS augmented by *ab intio* modelling. Moreover, the nuclear quantum character-dictated properties that would have escaped the scrutiny of the INS, could now be captured by the NCS technique. Motivated by these recent developments, in the present work, we provide a critical appraisal of the local structure and nuclear quantum dynamics in tungstic acid by means of a concurrent application of ND, INS, and NCS. Owing to the mass-selective nature of the NCS technique, we provide a more extensive view beyond the usual discussion of protons in confined water.

The work is organised in the following way. We provide a discussion of the benchmarking of the structural and dynamical information obtained from our diffraction and INS and NCS work against the results of the first-principles predictions. We conclude by providing a dis-cussion of the correlations between the elucidated structure and nuclear quantum dynamics of all constituent nuclei in the tungstic acid, with special emphasis on the local mobility of proton. We close by listing possible opportunities for further improvement of the experi-mental and computational protocol aimed at the mass-selective characterisation of NQEs in functional materials such as $WO_3 \cdot H_2O$.

2. Materials and Methods

The powder sample of $WO_3 \cdot H_2O$ was obtained from Sigma-Aldrich (99% purity, CAS 7783-03-1, LOT: 223328) and subjected to the neutron experiments at the ISIS Pulsed Neutron & Muon Source (Oxfordshire, United Kingdom). The collected data were reduced and processed within the Mantid software package.[42]

Neutron Diffraction

The low-temperature (T = 1.5 K) NPD experiment was performed on a high-resolution WISH diffractometer, installed at the ISIS Pulsed Neutron & Muon Source.[43] Data was grouped into five nominal diffraction angles (banks) and jointly refined using the JANA2020 program[44] according to the following procedure (and using JANA-specific parameters): (*i*) the background was fixed as a manual background selected by JANA program for each detector bank; (*ii*) the fractional coordinates were refined for tungsten and oxygen atoms; (*iii*) the isotropic displacement parameters were refined tungsten and oxygen atoms; (*iv*) the riding hydrogen model[45] was applied, which constrains hydrogen atom parameters to those of the non-hydrogen atoms (the O-H distance was constrained to 0.974 , the H-O-H bond angle to 110.78 degrees, and the isotropic displacement parameter of hydrogen atoms was scaled by a factor 1.2 with respect to its counterparts for tungsten and oxygen atoms); (*v*) the Lorentzian broadening parameters of the peak profiles were refined with asymmetry parameters fixed; (*vi*) preferred orientation was refined; (*vii*) the remaining experimental peak profile parameters were refined in the following order: (*a.*) T_{Zero} for banks 1 and 2, (*b.*) T_{Zero}, D_{IFA} and D_{IFC} for banks 3 and 4, while keeping the values of the parameters T_{Zero}, D_{IFA} and D_{IFC} for bank 5 at calibrated values, due to the fact that bank 5 represents the backscattering detectors with the highest resolution for diffraction.

Inelastic Neutron Scattering

The INS experiment was performed at the cryogenic conditions (T = 10 K) using the recently-upgraded TOSCA spectrometer.[46–50] The powder specimen was loaded into a rectangular Al sample cell sealed with In wire and cooled down to the base temperature. The high-resolution INS spectrum was analyzed up to 250 meV and further confronted with the INS spectra measured up to 600 meV on SEQUOIA (SNS, ORNL, US).[4]

Neutron Compton Scattering

NCS experiments were performed at the VESUVIO spectrometer installed at the ISIS Pulsed Neutron & Muon Source.[20,21,23,51–59] In order to standardise and facilitate the experimental and data treatment protocols, the same powder specimen and rectangular Al sample cells were used in both TOSCA and VESUVIO experiments. Additionally, in the case of the VESUVIO experiments, NCS spectra were recorded at 10, 50, 100, 200, and 300K, using a closed-cycle refrigerator stabilised setup, routinely applied at ISIS. A detailed description of the raw NCS data treatment is described elsewhere.[19,23,29–31,37,60,61] Thus, here we will only concentrate on the description of the main points.

The NCS spectra, recorded in the Time-Of-Flight (TOF) domain, were treated as a superposition of recoil peaks attributed to individual atomic species present in $WO_3 \cdot H_2O$. The Nuclear Momentum Distributions (NMDs), underlying the recoil peaks, were modelled as Gaussian functions with only ONE free fitting parameter per peak, the standard deviation of an NMD, hereinafter referred to as NMD widths. The ratios of the relative integral intensities of the recoil peaks were linearly constrained by the ratios of the number of atoms of a given type per formula unit multiplied by their total bound atomic cross-section values; a technique referred to as stoichiometric fixing.

Due to kinematic constraints imposed by the impulsive scattering within the Compton regime, the NCS spectra recorded in backscattering do not contain recoil peaks of hydrogen. For this reason, routinely, the data treatment protocol is broken down into two parts: (i) backscattering data treatment, followed by (ii) the treatment of NCS data recorded in forward scattering. In both cases, the treatment was performed sequentially, on the detector-by-detector basis.

The raw NCS data recorded in backscattering were subject to an iterative correction procedure. Within each iteration, for a set of fitting parameters (integral intensities and NMD widths), a multiple-scattering correction was simulated by Monte Carlo techniques and then subtracted from the raw data. The iterations were repeated until self-convergence

was achieved. The converged NMD widths of oxygen, tungsten, as well as aluminium from the sample container, were used as fixed parameters in the treatment of forward scattering data. Moreover, the NMD widths of oxygen and tungsten obtained from backscattering data treatment were used for the direct comparison with their counterparts obtained from *ab initio* modelling.

The iterative procedure of treatment of raw NCS data recorded by forward scattering detectors consisted of three steps per iteration: (*i*) initial fit of the sum of the recoil peaks in order to obtain a set of integral peak intensities and the NMD width value of the hydrogen with the NMD widths of other masses fixed at their final values obtained from backscattering data correction, (*ii*) the simulation of the multiple scattering, and (*iii*) the simulation of sample-dependent gamma background, both performed with the set of NMD widths and integral peak intensities as input parameters. The iterations were repeated until convergence was achieved.

Following the final iteration of data treatment in forward scattering, the recoil peaks of hydrogen were isolated by subtracting the simulated recoil peaks of other masses from the total signals on a detector-by-detector basis. The isolated hydrogen recoil peaks were individually transformed into the domain of the longitudinal momentum of the proton and focused. The focused hydrogen data were fitted by Gaussian NMD functions.

Ab initio Modelling

The electronic structure calculations were performed under Periodic Boundary Conditions (PBCs) starting with the crystallographic model of $WO_3 \cdot H_2O$ proposed by Szymański *et al.*[62] based on the room-temperature Single-Crystal X-Ray Diffraction (SXRD). The Plane-Wave Pseudo-Potential (PW-PP) formulation of Density Functional Theory (DFT) was employed as implemented in the CASTEP code (version 19.1).[63,64] Additional calculations were performed using CP2K[65,66] and CRYSTAL17[67] in order to check the reliability of the numerical procedure applied (e.g. the influence of the Exchange-Correlation (XC) functional beyond

semi-local formulations[67]).

In brief, in CASTEP, the Perdew-Burke-Ernzerhof (PBE) functional within the Generalized-Gradient-Approximation (GGA) was augmented with semi-empirical atom-pair-wise dispersion corrections from Tkatchenko and Scheffler (TS).[68] The core electrons were described by a set of hard, norm-conserving PPs, while the electronic wave functions were defined using a PW basis set with a kinetic energy cutoff of 900 eV. A Monkhorst-Pack grid was used to maintain a constant k-spacing of 0.05 Å^{-1}. The maximum G-vector of the fast Fourier transform (FFT) grid, G_{max} was defined as the 3/4 of the ideal grid size, and the fine-grid multiplier was set to 4. Variable-cell relaxation was performed under atmospheric pressure, imposing a three-point finite basis set correction. All structures were accurately relaxed to minimize the residual atomic forces. The convergence criteria in the variation of the self-consistent field (SCF), Hellmann–Feynman forces, and external stress were defined as 1×10^{-12} eV/atom, 1×10^{-5} eV/Å, and 0.0001 GPa, respectively.

Following geometry optimization, the vibrational response was explored using both harmonic Lattice Dynamics (LD) and *Ab Initio* Molecular Dynamics (AIMD) simulations. In the LD scheme, the phonon-dispersion relations were calculated across the First Brillouin Zone (FBZ) within the Density Functional Perturbation Theory (DFPT) in the reciprocal space formulation.[69–71] The Dynamic-Matrix (DM) was solved analytically at T = 0 K by relying on the primitive cell model. The phonon frequencies and eigenvectors were used to examine the mechanical stability of the starting model. The revealed imaginary modes were followed according to their eigenvector coordinates to find the minima on the multi-dimensional Potential Energy Surface (PES). The results of the LD simulations served as inputs for further predictions of the INS and NCS observables. The phonon eigenvalues and eigenvectors were used for direct simulation of the TOSCA spectrum.[72,73] The atom-projected vibrational densities of states (apVDOSs), obtained from the LD simulations, were also used for calculating the NMD widths of the atomic species (σ_j), according to the methodology extensively described elsewhere.[30,31,60]

9

A series of classical AIMD simulations following the Born-Oppenheimer approximation (BOMD) were performed at T = 10, 100, 200, and 300 K for a number of structural configurations considered. The term 'classical' signifies here that throughout the entire AIMD computational protocol, nuclei are treated as classical (i.e. point-like) particles. This implies that the AIMD trajectories are propagated using the classical (Newton) equations of motion with the forces that are however calculated on-the-fly by solving the electronic structure problem quantum-mechanically. This is an important limitation of the computational scheme, as it does not allow for phenomena such as nuclear quantum delocalisation or tunneling to be reproduced by processing the obtained trajectories of nuclear motion for individual nuclei. Moreover, as we shall see below, (see the discussion of the INS results below) such classical AIMD simulations are not capable of reproducing the effects of the zero-point energy (ZPE) on the nuclear dynamics. Thus, in this work, the classical AIMD simulations provide an additional layer of approximation of experimental results for the characterisation of the quantumness of nuclear species in tungstic acid beyond the harmonic framework.

The details of the classical AIMD simulation protocol are as follows. Supercell models of the size of 1×2×2 were used, reducing the k-point sampling to Γ-point. The basis-set quality and the numerical details were kept as described above, apart from the SCF convergence, which has been reduced to $\times 1^{-7}$ eV/atom, and the fine-grid multiplier was reduced to the FFT size. The AIMD simulations involved three stages. In the first step, each starting model was equilibrated for 6 ps under atmospheric pressure in the isothermal–isobaric ensemble (NPT). The Equations Of Motion (EOMs) were solved every 1 fs. The isotropic Andersen barostat was used along with a classical Nose-Hoover thermostat at a given temperature. At the second stage, the resulting configuration was confined in the average box derived from the NPT simulations, and 5 ps equilibration was performed in each case in the canonical ensemble (NVT). The time-step was reduced to 0.5 fs. Finally, the subsequent production run of 10 ps was performed in the microcanonical ensemble (NVE). To check the consistency of the AIMD predictions, the same set of calculations was also performed

10

using CP2K.[65,66] These calculations used PBE-D3(BJ)[74–77] in combination with plane-wave (400 Ry) / gaussian atom-centered double-zeta-quality basis sets (DZVP-MOLOPT) and Goedecker-Teter-Hutter (GTH) pseudopotentials. Convergence criteria were chosen to be consistent with the accuracy of the parallel calculations using CASTEP, showing that this approach provides a similar level of accuracy for both computational codes in line with our previous findings.[78,79] Finally, the CP2K simulations were extended by imposing Quantum-Thermostatting (QT-NVT) following a generalized Langevin equation (GLE) for two temperatures (T = 50 K and 300 K; stage (ii).[80,81] The system was equilibrated for 30 ps at target temperatures, providing the initial conditions for subsequent NVE trajectories. This simple approximation (hereafter referred to as the semi-classical approach) allowed us to extend the level of approximation beyond the classical AIMD simulations and include the effects of ZPE in the decription of nuclear quantum effects in tungstic acid.

The production-run trajectories served as input for the modelling of the apVDOSes *via* the explicit calculation of the Velocity AutoCorrelation Function (VACF). The VDOS for a particular atom j was evaluated, according to the standard expression, as the Fourier-transform of its VACF:

$$VDOS = \sum_j^N \int_0^\infty \frac{<\nu(t)_j \nu(0)_j>}{<\nu(0)_j^2>} exp\left(-i\omega t\right) dt, \tag{1}$$

where $\nu(t)_j$ is the velocity at time t. The analysis and the post-processing of the BOMD production runs was made with the help of the TRAVIS code.[82,83] Alternatively, a recently implemented strategy was used to model the INS spectra from MD trajectories by means of an approximate treatment of the Debye-Waller factor which accounts for overtone and combination bands, as well the specific configuration of the TOSCA spectrometer.[84] The apVDOSs were further used for calculating σ_j, for a direct comparison with the values of the NMDs widths obtained from the LD calculations and directly from the NCS experiments.[29,31,37,60,85]

3. Results and Discussion

Crystal Structure

In what follows, we provide a description of the crystal structure elucidation procedure that was adopted for $WO_3 \cdot H_2O$. Importantly, as already mentioned in the Introduction in the context of our global multi-technique approach, NPD experiments alone cannot provide an unambiguous answer in terms of best structural model that would be also compatible with the local structure and dynamics. Rather than that, the analysis of diffraction data provides the first exploratory step, serving as the source of candidate structural models to be further examined by the INS and NCS techniques and contrasted against the results of *ab initio* simulations. In this spirit, at this stage of the analysis of experimental data, we do not intend to provide a definite solution, but rather discuss drawbacks of the existing models and point out towards better solutions.

The tungsten trioxide has several hydrated forms ($WO_3 \cdot xH_2O$), each one having a layered structure.[86] The crystallographic structure of $WO_3 \cdot H_2O$ was originally solved at ambient conditions by Szymański *et al.*,[62] using a single-crystalline mineral specimen. The solution yielded an orthorhombic structure, being defined by the *Pbnm*-(D_{2h}^{16}) space group. By convention, from here onward we refer to standardized isomorphous *Pnma*-(D_{2h}^{16}) representation, which can be achieved by altering the *Pbnm* structure as follows:

$$Pbnm \rightarrow \begin{bmatrix} 0 & 1 & 0 \\ 1 & 0 & 0 \\ 0 & 0 & -1 \end{bmatrix} \rightarrow Pnma \tag{2}$$

No information on the low-temperature structure has been available to date. To fill this gap, we have performed high-resolution NPD experiments. Figure 1 shows an example of the Rietveld refinement of the experimental data collected at T = 1.5 K leading to the orthorhombic structure, refined in the *Pnma* space group with the goodness-of-fit parameter
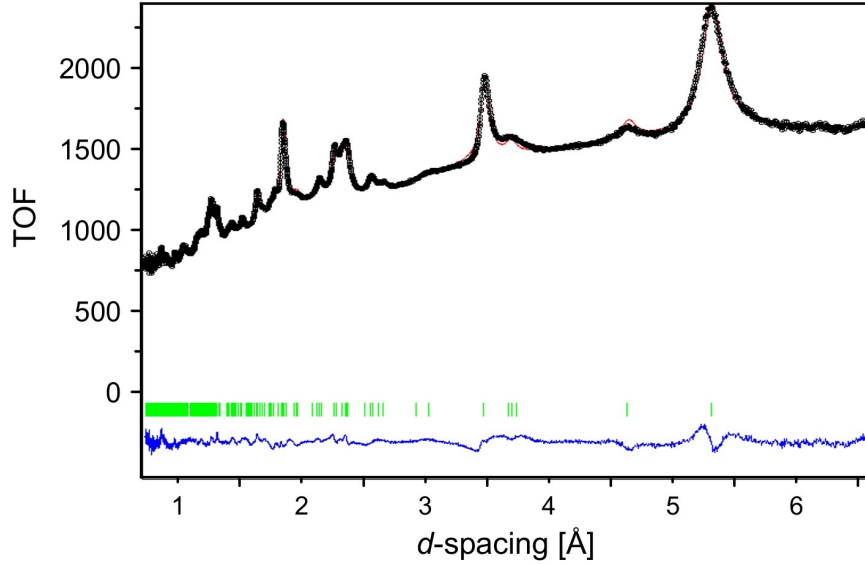
Figure 1: Rietveld refinement (using the *Pbnm* space group) of the ND patterns of powder $WO_3 \cdot H_2O$ specimen, collected at T = 1.5 K on the WISH diffractometer (ISIS, STFC, UK). The black points refer to the experimental data. The red and blue lines indicate the refined fit of the data and the difference between fit and experiment, respectively. Green bars denote the expected reflexes according to the adopted crystallographic model.

of 3.3719. For all structural models tested, the NPD profiles recorded up to the Room Temperature (RT) did not require any model change when the refinement was performed as a function of temperature. Hence, it can be concluded that no phase transition occurs between 1.5 K and Room Temperature (RT) and therefore the crystal structure originally proposed by Szymański[62] can be used as a starting model. However, as described in the Materials and Methods section, the entire NPD refinement procedure is a complicated interplay of optimisation of the crystal structure, the signal background, the local-disorder induced broadening of peak profiles, as well as the experimental peak profile shapes specific for neutron spallation sources. Due to these reasons, a great degree of cross-correlation of refinement parameters exists which is accompanied by a complicated behaviour of a variety of fit-quality factors used. In the case of the *Pnma* structure under consideration, a Le Bail profile fit was initially carried out and the peak profiles were found to be broadened compared to the instrument resolution and could be modelled by a Lorentzian profiles. This broadening can be due to the particle size or internal strains with the former more likely. This, combined with the

13

complicated nature of the NPD background, has led to a situation in which some refinement quality indicators seem to favour $Pnma$ structure and some favour another candidate structure described by the $P2_1P2_1P2_1$ space group. (The CIF files as well as all the parameters characterising the goodness of fits used by the JANA program in the case of the structural models refined within the $Pnma$ and $P2_1P2_1P2_1$ space groups were included in the SI.) The refinement of the NPD data using the $P2_1P2_1P2_1$ space group leads to the goodness-of-fit parameter of 2.8649, thus superior to the one obtained for the $Pnma$ structure (see Table 2 in the SI). Thus, in what follows, we will subject both structural models to further scrutiny by examining their feasibility in light of the results of *ab initio* simulations.

Table 1: Alternative models of the crystal structure of $WO_3 \cdot H_2O$ according to experimental data (SXRD, PXRD – ambient conditions, RT; and , and NPD – low-temperature, 1.5 K) and plane-wave GGA-DFT-D modelling (total-energy optimization at 0 K). The NPD refinement provided two alternative structural models within the $Pnma$ symmetry. The $Pnma$-alt model was obtained by an unconstrained refinement, resulting in a considerably different internal structure (see the SI). For each theoretical model the phonon dispersion relations were calculated. The imaginary modes detected in the vicinity at / or around the Γ-point are consequently labelled as $(i–ix)$, with the imaginary eigenvalue given in meV for a considered wavevector $[q_a, q_b, q_c]$. Relative difference in lattice-energy per $WO_3 \cdot H_2O$ unit (ΔE^{DFT}) is provided w.r.t the lowest-energy model, which was found fully mechanically-stable, i.e. $^{(ii)}P2_1P2_1P2_1$. Note that all the models considered are orthorhombic but the $^{(iii)}P2_1/c$ structure $(\beta = 89.3°)$.

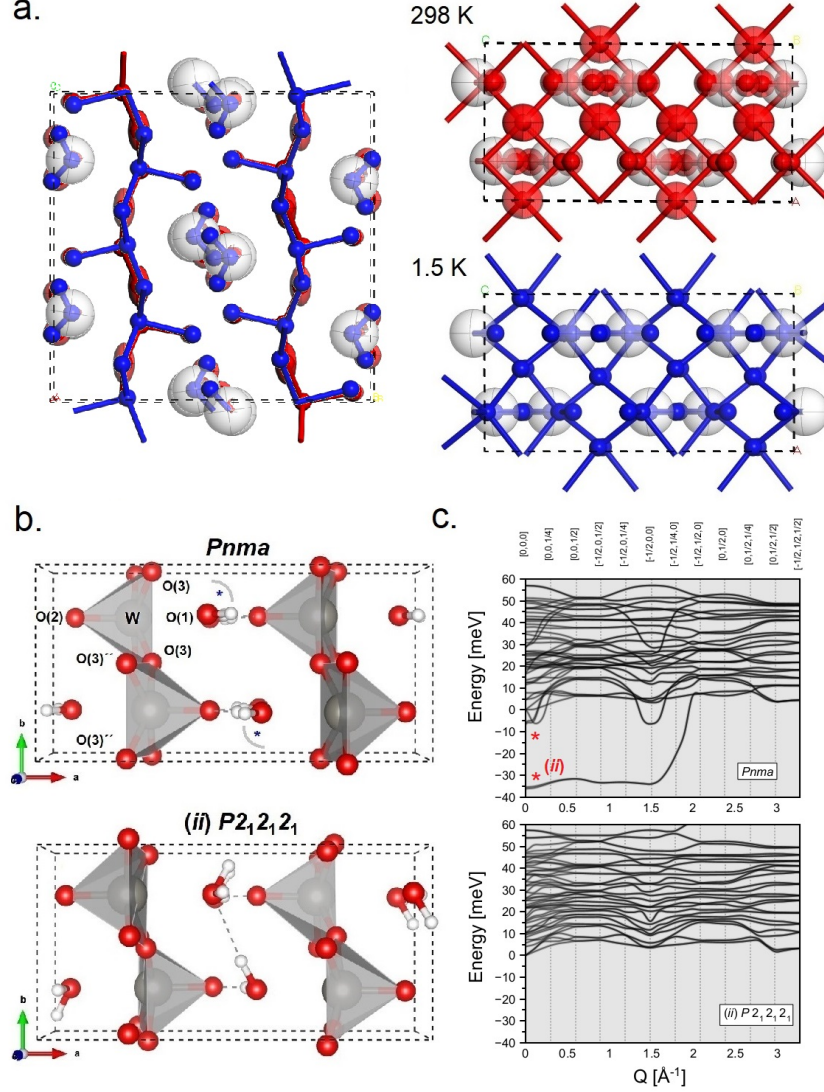| Temp.	Model	Imaginary Modes	ΔE^{DFT}	Cell Parameters			
	[Space Group]	$[q_a,q_b,q_c]$	[kJ/mol]	a [Å]	b [Å]	c [Å]	V [Å^3]
RT Ref.[62]	$^{(SXRD)}Pnma$	–	–	10.711	5.249	5.133	288.59
RT Ref.[87]	$^{(PXRD)}Pnma$	–	–	10.735	5.252	5.138	289.68
1.5 K	$^{(NPD)}Pnma$	–	–	10.641	5.242	5.155	287.55
1.5 K	$^{(NPD)}Pnma$-alt	–	–	10.654	5.244	5.148	287.62
0 K	$Pnma$	$(i)[0,0,0] = -36.2$ meV $(ii)[0,0,0] = -35.5$ meV $(iii)[0,0,0] = -6.7$ meV $(iv)[0,0,0] = -6.1$ meV $(iv)[0,0,0] = -6.1$ meV $(v)[0,0,0.0833] = -6.0$ meV	7.07	10.83	5.37	5.17	300.76
0 K	$^{(i)}Pna2_1$	*fully-stable*	0.95	10.64	5.31	5.31	299.98
0 K	$^{(ii)}P2_12_12_1$	*fully-stable*	0.00	10.69	5.28	5.27	297.42
0 K	$^{(iii)}P2_1/c$	$(vi)[0,0,0] = -26.3$ meV $(vii)[0,0,0] = -26.3$ meV	5.62	5.33	5.12	10.86	296.35
0 K	$^{(iv)}P2_12_12_1$	$(viii)[0,0,0.3333] = -5.6$ meV	0.33	10.70	5.27	5.28	298.16
0 K	$^{(NPD)}Pnma$-alt	$(ix)[0,0,0.0833] = -5.0$ meV	10.18	11.44	5.33	5.13	312.74

Figure 2: (a.) Ball-and-stick projection of the crystallographic structure of $WO_3 \cdot H_2O$ (orthorhombic *Pnma*) in two alternative perspectives, according to SXRD (298 K; red) and NPD (1.5 K; blue) diffraction experiments.The atoms from each structure are discerned with red and blue colors and the water molecules are marked with transparent spheres. Note visibly larger thermal displacement parameters on the oxygen atoms at ambient conditions according to the SXRD study. (b.) The structural models of relevance to this work were obtained with solid-state DFT calculations following the LD calculations of the phonon structure. Note a different orientation of water molecules in both models, and the respective transformation marked with the asterisks in the *Pnma* model. (c.) Phonon dispersion relations below 60 meV according to the LD calculations at 0 K. Note the branches with imaginary eigenvalues marked with the asterisks for the *Pnma* structure. The zone-center mode marked as (*ii*) has been followed to obtain a fully mechanically-stable orthorhombic structure with $P2_1P2_1P2_1$ symmetry).

15

The refined low-temperature structure is presented in Figure 2 (a.) and compared to the ambient-temperature model from Szymański *et al.*,[62] adopting the standardized *Pnma* convention. The quantitative comparison with the XRD data for single-crystal (SXRD) and powder (PXRD) specimens can be found in Table 1. The structure of $WO_3 \cdot H_2O$ is characterized by distorted octahedral units formed by tungsten atoms coordinated by five oxygen atoms and a water molecule. These octahedra share four corners in the equatorial plane to form sheets with water intercalated in between. The low-temperature structure only shows a tiny unit-cell compression, with the cell volume reduced by 1 $Å^3$, suggesting that tungstic acid as a material is rather stiff. The long cell-axis reduces by less than 0.05 Å. Since the interlayer spacing is defined by water arrangement, no considerable temperature-induced configuration rearrangement is expected. The structure from Szymański *et al.*[62] shows noticeable thermal ellipsoids on oxygen atoms, which are due to the thermally-activated torsional motion of the polyhedra in the equatorial plane. According to our refinement of the NPD data, this type of motion is hardly observed at 1.5 K. This effect is manifested by very slight changes in the *b*- and *c*-axes by no more than 0.02 Å. These minor structural differences show that there is no structural phase transition expected below RT, and the water remains visibly confined all across the range T = 1.5 – 300 K. The *Pnma* model shows that there are no interactions between the water molecules, which are solely H-bonded to the two neighbouring polyhedra and perfectly aligned along the *ca*-mirror-plane. This has been clearly illustrated in Figure 2 (b.)

As mentioned in the Introduction, the analysis of the ND data is not suitable for the characterisation of the local structure and dynamics, and can only be used to elucidate the long-range order. Thus, in order to capture those structural and dynamical features that escape the scrutiny of the ND, but play a crucial role in the selection of the structural model that best describes the tungstic acid, both at the local and global scale, following the ND analysis, we have performed theoretical calculations to characterize the structure and mechanical stability of the *Pnma* model under ambient pressure. The results of this

analysis are presented in detail in Table 1. An extensive benchmark of alternative theoretical approaches can be found in the SI. The calculations within the $Pnma$ model using semi-local dispersion-corrected DFT (PBE-TS) provide a reasonable description of the structure. These calculations also allow to rule out an alternative model of the $Pnma$ structure proposed as the outcome of the unconstrained NPD analysis (hereafter, $Pnma$-alt).

We have examined the mechanical stability of the $Pnma$ model by calculating phonon dispersion relations. In the calculations, we have set very strict optimisation criteria, in order to rule out the influence of numerical errors. The resulting phonon structure in the low-energy part (below 60 meV) is displayed in Figure 2 (c.), showing that $Pnma$ model is highly-mechanically unstable. Several imaginary phonon branches have been found, with negative eigenvalues occurring already at the Γ-point. The imaginary phonon energies are collected and labelled in Table 1. Apart from the potential breakdown of the harmonic approximation due to a presumably soft-binding potential of water, this picture clearly shows that the $Pnma$ model does not correspond to the true minimum on the multi-dimensional potential energy surface (PES) of the crystal. The imaginary phonon branches are spanned far beyond the Γ-point, suggesting that the water molecules must be far more correlated than assumed within the $Pnma$ model (with no intermolecular bonding). In search of the preferable water orientation corresponding to the real stationary points on the multi-dimensional PES, we have followed the eigenvectors of four zone-centre imaginary modes (labelled as modes no. (i–iv) in Table 1.) and reduced the symmetry accordingly. As a result, we have found two structures, which are fully mechanically stable and nearly iso-energetic. The structures are labelled as $^{(i)}Pna2_1$ and $^{(ii)}P2_12_12_1$. These are visualized in Figure S1 in the SI and provided as CIF files. The estimated difference in the lattice energy per formula unit is below 1 kJ/mol. The structures differ in the mutual orientation of the H_2O molecules in the neighbouring inter-layer space, accompanied by tilting of the distorted octahedral units. While there is no direct correlation between water in the neighbouring layers, their mutual orientation depends on the octahedral tilting. Further insights into the structural properties

17

have been inferred from the analysis of the low-temperature INS experiments contrasted with the *ab initio* predictions.
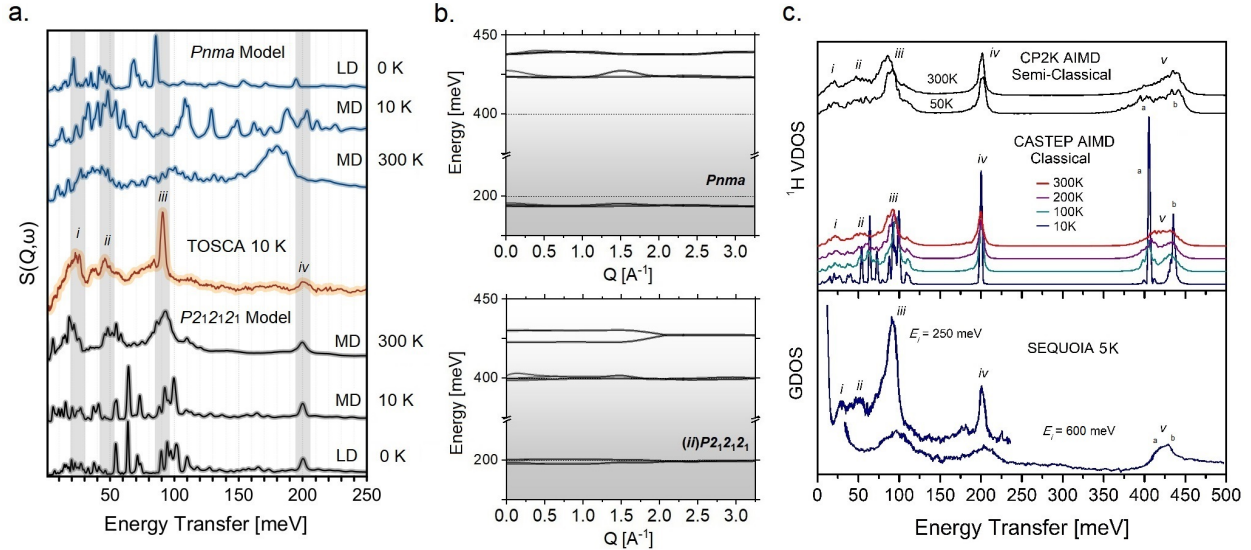

Figure 3: (a.) Experimental high-resolution INS spectrum of $WO_3 \cdot H_2O$ recorded on TOSCA at 10 K and presented in the energy transfer range of 2–250 meV. The experimental spectrum is compared to the results of the theoretical predictions using the *Pnma* and $P2_1P2_1P2_1$ models, respectively. The theoretical spectra marked as LD have been obtained from lattice-dynamics simulations at 0 K and account for the mode dispersion. MD stands from the results of AIMD simulations at finite temperatures (10 and 300 K, respectively). The simulated INS spectra take into account configuration of the TOSCA spectrometer.[84] (b.) Phonon dispersion relations for $WO_3 \cdot H_2O$ over the energy-range of 150–450 meV, according to the harmonic LD calculations performed at 0 K for the two models under consideration. (c.) The experimental INS spectra of $WO_3 \cdot H_2O$ collected at 5 K on a direct-geometry SEQUOIA spectrometer, using two different incident-energies, $E_i = 250$ and 600 meV, respectively.[4] The experimental spectra are compared to the results of the classical and semi-classical AIMD simulations at selected temperatures. See main text for details. The theoretical spectra are presented in the form of ^{1}H VDOS for a direct comparison with SEQUOIA. The labels in the figures (*i–v*) denote characteristic vibrations of water molecules. Adapted with permission from [Mitchell *et al. ACS Energy Lett.* 2019, 12, 2805–2812]. Copyright [2021] American Chemical Society.

Inelastic Neutron Scattering

A high-resolution INS spectrum of $WO_3 \cdot H_2O$, recorded with an indirect-geometry TOSCA instrument, has been displayed in Figure 3 across the energy transfer range 2 — 250 meV. The spectrum has been contrasted with the results of the first-principles predictions using

both *Pnma* and $P2_1P2_1P2_1$ configurations. By comparing the zero-temperature harmonic LD spectra, we note that both models allow for a quantitative description of the INS data. However, only the mechanically-stable $P2_1P2_1P2_1$ structure provides physically meaningful normal modes. The TOSCA spectrum reveals fours characteristic spectral regimes, marked with shaded vertical areas and labelled as (*i–iv*). To discern between the fundamental and higher-order transitions, we have performed decomposition of the theoretical TOSCA spectrum presented in Figure S2. The lowest energy regime is due to external modes, where large-amplitude deformations of the inorganic framework involve water motions of translational nature, giving rise to a considerable spectral intensity (*i*). Water librations, primarily involving the water torsional motion around the W...O axis, contribute at around 50 meV (*ii*). Transverse H-bond deformations, γ(H...O), are observed at around 100 meV (*iii*), and in-plane δ(H$_2$O) modes contribute to well-defined feature at ca. 200 meV. First-principles calculations have also been performed for the second lowest-energy configuration, ($Pna2_1$), as reported in Figure S1 of the SI. We have found that both $P2_1P2_1P2_1$ and $Pna2_1$ retain the same nature of the water vibrations, with the characteristic spectral patterns predicted at very close energy transfers, however, revealing some differences in the intensity distribution (see e.g. the spectral intensities for the γ(H...O) deformations at around 100 meV). By further comparing the outputs for *Pnma* and $P2_1P2_1P2_1$ structures, we note that both models predict the transition energies with opposite errors. The *Pnma* structure shows downward shifts in the positions of the bands (*iv*) and (*iii*), due to the presence of underbonded, non-interacting water molecules. Furthermore, the mechanical instability of the structure results in a substantial number of imaginary librational modes. Moreover, as a consequence of mode coupling, all the modes coupled to the librational modes, are distorted. On the contrary, the physically-meaningful $P2_1P2_1P2_1$ model provides a reasonable match to the experimental data. However, the LD calculations, being harmonic in nature, find the confining potential too stiff, resulting in visibly upward shifts for the modes below 120 meV. This artefact is particularly severe for the modes (*iii*), mainly related to the τ(H$_2$O) motion.

In order to go beyond the picture provided by the harmonic lattice dynamics and shed more light on the extent of disorder present in $WO_3 \cdot H_2O$, we have performed a set of extensive AIMD simulations and validated the results against the experimental INS data (see Figure 3). The results of the 10 K NPT MD simulations for selected structural models are presented in Figure S3 in the SI, with the lowest energy configuration ($P2_1 P2_1 P2_1$) marked as (a.). The low-temperature MD simulations confirm that the crystallographic $Pnma$ structure (marked as (b.) in Figure S3 in the SI) is not stable, and once the symmetry constraints are not imposed it immediately evolves toward the lowest-energy configuration. However, starting from the high-symmetry $Pnma$ initial structure, the system becomes trapped in a slightly disordered configuration, destabilized by ca. 2.5 kJ/mole per formula-unit w.r.t. the lowest-energy one (a.). It is important to note that the resulting structure is described by randomly oriented water molecules and represent the case where the close spatial correlation of water within layers is lost.

According to Figure 3, the low-temperature MD simulations relying on the $P2_1 P2_1 P2_1$ model provide an INS spectrum nearly identical to the harmonic one obtained for the above-discussed alternative low-energy configuration (see $Pna2_1$ in Figure S1 of the SI for comparison, and Figures S4–S5 proving energy stability and convergence). Thus, the differences in the intensity distribution in the INS spectra simulated for the two lowest-energy configurations, discussed above, come from the symmetry constraints affecting the geometry of the inorganic framework and preserving the octahedra tilting. The INS spectrum derived from the simulations within the $Pnma$ model completely fails in describing the experimental data. This shows that water in $WO_3 \cdot H_2O$ has to be ordered and spatially-correlated within the layers, ruling out the presence of an amorphous, or randomly ordered water molecules. Other alternative models examined here (e.g. (c.) and (d.) presented in Figure S3, SI) are considerably off the potential minimum and provide INS spectra which do not match the experimental data. Therefore these models have been excluded from further discussion. The existence of disorder in $WO_3 \cdot H_2O$ cannot be completely ruled out, however. Disorder,

e.g., related to formation of domains, can still exist on spatial scales beyond 1 nm, and thus beyond the the spatial scale of our first-principle simulations.

Figure 3 (a.) compares the results of AIMD simulations obtained at 300 K. While the disordered model derived from the *Pnma* structure completely fails in describing the experimental data, the $P2_1P2_1P2_1$ model provides a superb description of the INS spectrum. Most importantly, clear downward shifts of the features below 100 meV toward the experimentally observed energy transfers show that the water-confining potential is very soft. The position of the $\delta(H_2O)$ feature (*iv*) is, nevertheless, hardly affected by the temperature, which means that the anharmonicity is closely related to the transverse motions along the W...O coordinate. However, the simulations at 300 K tend to broaden the $\gamma(H...O)$ feature at ca. 100 meV. On the whole, the small inaccuracies present in AIMD simulations are the consequence of the fact that sampling of the anharmonic part of the PES requires the use of effective classical temperature to account for zero-point motion.[78,88] A similar strategy (AIMD with VASP at 300 K) has been adopted by Mitchell et al., allowing to successfully describe the signatures of proton intercalation in the low-temperature INS spectra.[4] The need of incorporating an effective temperature in classical MD simulations is a well-recognised issue, and for hydrogen motions, this may require the use of temperatures as high as 600 K.[89] However, since all the atoms in the system, including tungsten, are subjected to the same classical temperature, setting the temperature of the simulations well above this limit will result in altering the dynamics of the whole ensemble. Thus, as a matter of compromise, we do not change the strategy for the AIMD simulations; however, recognising the limitations of the methodology adopted herein.

Before we delve into the interpretation of the INS spectra recorded on tungstic acid, the following general remark is in order. The intensity of an INS band is proportional to the product of the incoherent scattering cross-section and the amplitude of vibration and is damped by the Debye–Waller factor.[21,90] On indirect-geometry instruments, where the instrument trajectory essentially follows the hydrogen recoil line, the higher the frequency of

the observed vibrational mode, the larger the magnitude of the Debye–Waller factor and thus the more the intensity of the mode is damped.[21,90] Thus, on an instrument such as TOSCA, at energy transfer <1200 cm^1, the spectrum is well defined, but at larger energy transfers, including the O-H stretch regime, the details of bands are washed out.[21,90] In parallel, the intensity of the higher order transitions, become significant at large Q. The combination of these two processes renders them hardly detectable.[90] This has been illustrated in Figure S2, showing decreasing fundamental intensities above 100 meV and enhanced contributions from higher order transitions. The problem with the interpretation of the high-energy part of the INS spectra can be, however, circumvented by referring to the experimental data obtained using a direct-geometry instrument. To this end, we will use the INS data on tungstic acid reported by Mitchell *et al.*[4] Figure 3 (b.) compares the dispersion relations predicted for both *Pnma* and $P2_1P2_1P2_1$ models using harmonic LD at 0 K. As expected, intermolecular interactions present in the latter model shift the $\delta(H_2O)$ mode upwards while lowering the energy of the $\nu(OH)$ stretch mode, the effect which can be confronted with experimental data reported by Mitchell *et al.*[4] The low-temperature (5 K) INS spectrum recorded on SEQUOIA with two incident-energies ($E_i = 250$ and 500 meV) allows to cover the energy transfers up to 500 meV. This has been displayed in Figure 3 (c.) and compared to the results of variable-temperature classical and semi-classical AIMD simulations performed using CASTEP and CP2K, respectively (see section Methods for more details). Owing to a direct-geometry configuration of SEQUOIA, the spectral intensity at high energy transfer values is not subjected to damping as in the case of TOSCA. However, the spectral resolution considerably decreases while going away from the incident-energy. Therefore, SEQUOIA provides here more insights to higher-energy transitions, uncovering better-resolved $\delta(H_2O)$ mode at ca. 200 meV and allowing to detect the $\nu(OH)$ stretch (hereafter, (v)) for further validation of the first-principles simulations.

The AIMD simulations allow identifying the hydrogen motions in tungstic acid that are sensitive to temperature and, hence, reveal a pronounced anharmonicity. This particularly

refs to modes (ii), (iii), and (v). As shown in Figure 3 (c.), the effective temperature of 300 K, adopted for the AIMD simulations, allows to properly describe the INS spectrum of tungstic acid over the entire energy-transfer range. However, in order to account for the combined effect of anharmonicity and nuclear quantum nature of the hydrogen manifested in the form of the zero-point energy, one has to apply in AIMD simulations an effective temperature which is a function of the mode frequency, a technique referred to as quantum thermostatting.[78,79] Thus, in our AIMD simulations, we have augmented the classical AIMD simulation by applying two different quantum thermostatting schemes, hereinafter referred to as semi-classical simulations. Both of them allow for the presence of a coloured noise reproducing the power spectral density of a quantum harmonic oscillator, and both result in INS spectra of very similar quality.[78,79] We have considered two temperature conditions, the lowest-accessible temperature for the simulations, 50 K, and 300 K. Inspection of Figure 3 (c.) confirms that earlier-discussed broadening of the band (iii) is an artefact stemming from the use of the same effective temperature for all degrees of freedom. The use of quantum thermostatting allows circumventing this issue, properly describing the INS spectrum already at 50 K. The experiments find the centre of gravity of the (iii) band at 91 meV, and both classical (300 K) and semi-classical (50 K) simulations predict the transition at 91–92 meV. However, we note that according to semi-classical simulations at 300 K, this band is further shifted down to 86 meV, which is not the case for other motions, e.g. bands (i), (ii), and (iv). Interestingly, this further supports earlier findings from INS experiments above the room temperature. Daniel et $al.$ have reported the INS spectrum of $WO_3 \cdot H_2O$, measured at 348 K on IN6 (ILL, Grenoble, FR), with the (iii) band observed at 95 meV, that is in perfect agreement with our semi-classical simulations at the room temperature.[86] This observation is of importance for supporting the validity of the presented model of the local structure of tungstic acid at ambient conditions, showing that water remains confined well above the cryogenic conditions.

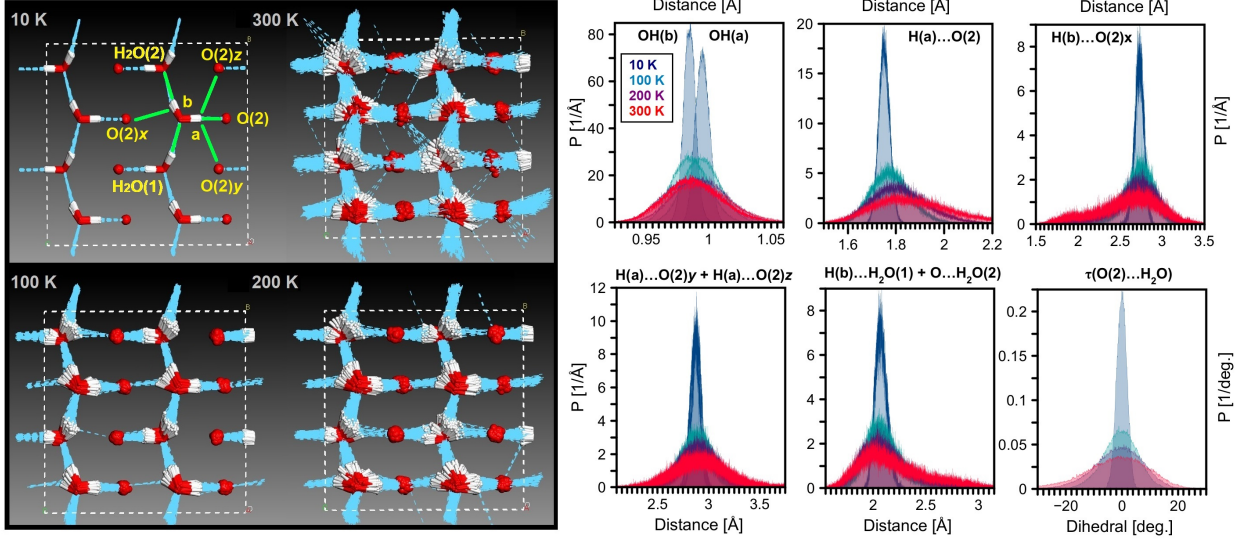The approximate semi-classical simulations of the $\nu(OH)$ stretch regime are of limited

Figure 4: (left panel) The cumulative time-dependent structures of $WO_3 \cdot H_2O$ obtained from temperature-variable classical AIMD simulations at 10, 100, 200, and 300 K, respectively. The hydrogen-bonds detected with the $r(H...O)$ cutoff of 2.2 Å are are drawn as light-blue dashed lines. The most-relevant close contacts are marked with green lines on the 10 K structure and labelled in yellow. (right panel) Analysis of selected structural parameters in function of classical temperature.

trust due to the numerical artefact, referred to as potential Zero-Point Energy Leakage (ZPEL) .[91] Therefore, in our further discussion we focus on classical AIMD results. By comparing the SEQUOIA data in the upper limit of the energy transfers (Figure 3 c) with the harmonic phonon picture (Figure 3 a) we find that the 0 K $P2_1P2_1P2_1$ model improperly predicts the presence of two well-separated $\nu(OH)$ band components, centered at ca. 400 and 430 meV. The INS spectrum shows an asymmetric band with underlying contributions centred at ca. 420 (a) and 430 meV (b), whereas the lower-energy feature is visibly broadened. This effect has been accounted for by classical AIMD simulations, where the respective features evolve with temperature from 405 and 435 meV (at 10 K) to 415 and 430 meV (at 300 K). To understand the origin of this effect, we refer to Figure 4, where selected structural parameters are displayed as a function of temperature. The analysis reveals that each H_2O is engaged in manifold close-contacts (within 3 Å) with both other water molecules and O=W fragments. The analysis of the $r(O-H)$ bond-lengths shows their inequivalence at 10 K and suggests stronger bonding to neighbouring O=W fragments. The hydrogen

24

atoms marked as (a), show two r(H...O) close-contacts within c.a. 2.9 Å(i.e. O(2)y and O(2)z); and one stronger r(H...O) interaction (i.e. with O(2) within c.a. 1.8 Å). Therefore, this expresses as the lower-energy ν(OH) component in INS spectrum. The hydrogen atoms marked as (b) interact with neighboring H_2O (r(H...O) within c.a. 2.2 Å) and with O=W fragment (O(2)x within c.a. 2.7 Å). A detailed structural analysis presented in Figure 4 suggests that zero-point motion reduces inequivalence between protons (a) and (b), which is directly supported by the respective ν(OH) band visible in experimental INS spectra. Concomitantly, the H(a)...O(2) is weakened, and the (a) component in the INS spectrum is upward-shifted. At this point, it is instructive to compare our low-temperature AIMD simulations with the AIMD simulations provided by Mitchell et al.[4] (see black curve in Fig. 4 (d) in Ref [4]). Qualitatively, both sets of simulations draw a similar picture. In the latter case, the (OH) stretching mode (v) appears as assymetrically broadened suggesting no signs of splitting due to inequivalence between protons (a) and (b). However, the difference in the stretching regime can be attributed to different numerical scheme adopted in both sets of calculations as we have earlier illustrated its sensitivity to basis-set definition and the empirical dispersion-correction scheme.[60,78] By influencing the position of both components to the band (v) it affects the total envelope of the ν(OH) band. We further note that the structural models reported by the authors further deny the water orientation defined by the symmetry constraints of the *Pnma* model, in line with our findings, with a high propensity of hydrogen-bond formation with other water molecules.

On the whole, our analysis suggests that the more distant contacts with the O(2)y and O(2)z moieties remain hardly affected. Simultaneously, the interactions of protons (b) with neighbouring H_2O molecules are strengthened as a consequence of the zero-point motion. As evident from the cumulative time-dependent structures presented as cartoons in Figure 4, along with the presence of additional peaks in the structural probability distributions, the H_2O molecules become spatially delocalised. This observation is in line with the anharmonic potential associated with the modes below 100 meV. This approximate picture of nuclear

quantum dynamics appears fully consistent with the INS data, suggesting that H_2O has a great deal of conformational freedom. This finding is in line with the result by Mitchell et al.[4] obtained from the analysis of the QENS and solid-state NMR data, that there is no significant translational motion of water in $WO_3 \cdot nH_2O$ on a time scale relevant to liquid-like water diffusion but conformational freedom is allowed. It is worth noting here, that wereas the QENS and ss-NMR probe molecular motion on the time scales from picoseconds to nanoseconds, the INS technique as well as the AIMD simulations probe water motion on the femtosecond timescale. Moreover, the NCS technique probes the quantum character of the nuclear degrees of freedom, i.e., the extent of the nuclear wavefunctions characterised by the widths of the nuclear momentum distribution, and thus, by virtue of the uncertainty principle, the spatial extent of the wave functions of the protons and oxygen atoms in water. On the whole INS, AIMD and NCS, probe the spatial extent of delocalisation that is commensurate with the amplitude of vibrational displacements of H and O, and thus fundamentally different from the spatial scale of rotational and translational diffusion.

We close our discussion by comparing INS data recorded for tungstic acid and water in different confining environments. On the whole, the INS spectrum of $WO_3 \cdot H_2O$ is shown to be similar to its counterpart in hexagonal ice but it supports on-average weaker hydrogen bond network. The observed stretch mode energies (420–430 meV) are greater than that of ice-Ih (406 meV).[8] Interestingly, the INS spectrum of tungstic acid is nearly identical to that of water in Single-Walled Carbon Nanotubes (SWNT).[8] This is in-line with finding that our model of H-bonding network to some extent resembles the models of shell-molecules at the walls of SWNT.[8] A comparison of the stretching regimes in the INS spectra of tungstic acid and water in SWNT shows that in the latter case the band profile is more symmetric, which is in line with two different types of H-bonds in $WO_3 \cdot H_2O$. The $\nu(OH)$ band is found at 422 meV, which supports a similar strength of the specific interactions in these systems.

Neutron Compton Scattering

NCS spectra of $WO_3 \cdot H_2O$, collected at T = 10 K (panels a, b, and c) and at T=300 K (panels d, e, and f) on the VESUVIO spectrometer (ISIS, STFC, UK), are shown in Figure 5. Owing to the technique of stoichiometric fixing, in the backscattering detection regime, a clear mass separation is visible for the recoil peaks of the oxygen (blue shaded areas in panels a and d), aluminium container (magenta shaded areas in panels b and d), and tungsten (orange shaded areas in panels a and d). In the forward scattering regime, a very good separation of recoil peaks is clearly visible between the recoil peak of the hydrogen (grey shaded areas in panels b and d), and the combined recoil peak of the oxygen, aluminium container, and tungsten. This allows a clean subtraction of the composite peak from the total forward scattering NCS signal with the aim of isolating the hydrogen recoil peak and transforming it into the longitudinal momentum space of the proton, depicted in panels c and f together with the average proton resolution function in the longitudinal momentum space , i. e., the space of all possible values of the projection of the proton momentum on the direction of the neutron momentum transfer vector (blue shaded areas in panels c and f). As can be seen in panels c and e, satisfactory fits of Gaussian underlying momentum distributions are obtained at both T = 10 K and T=300 K (see solid red lines in panels c and f).

The results of the benchmarking of the NMD widths of the protons in $WO_3 \cdot H_2O$ against the predictions obtained from *ab initio* LD and BOMD simulations are depicted in the lower panel of Figure 6. As can be clearly seen, the NMD width values obtained from the experiment are clearly ca. twenty per cent below the *ab initio* predictions obtained for both crystal phases in the limit of 0K, and the discrepancy between the theory and experiment decreases with increasing temperature. At the room temperature, however, the experimental values are still ca. 10 per cent below the predictions. Interestingly, the predictions obtained from BOMD simulations for the $P2_12_12_1$ phase of $WO_3 \cdot H_2O$ are closer to the experimental values than the predictions obtained from the LD simulations starting from 100 K. This behaviour is mostly related to the failure of the LD to account for the inherent anharmonicity
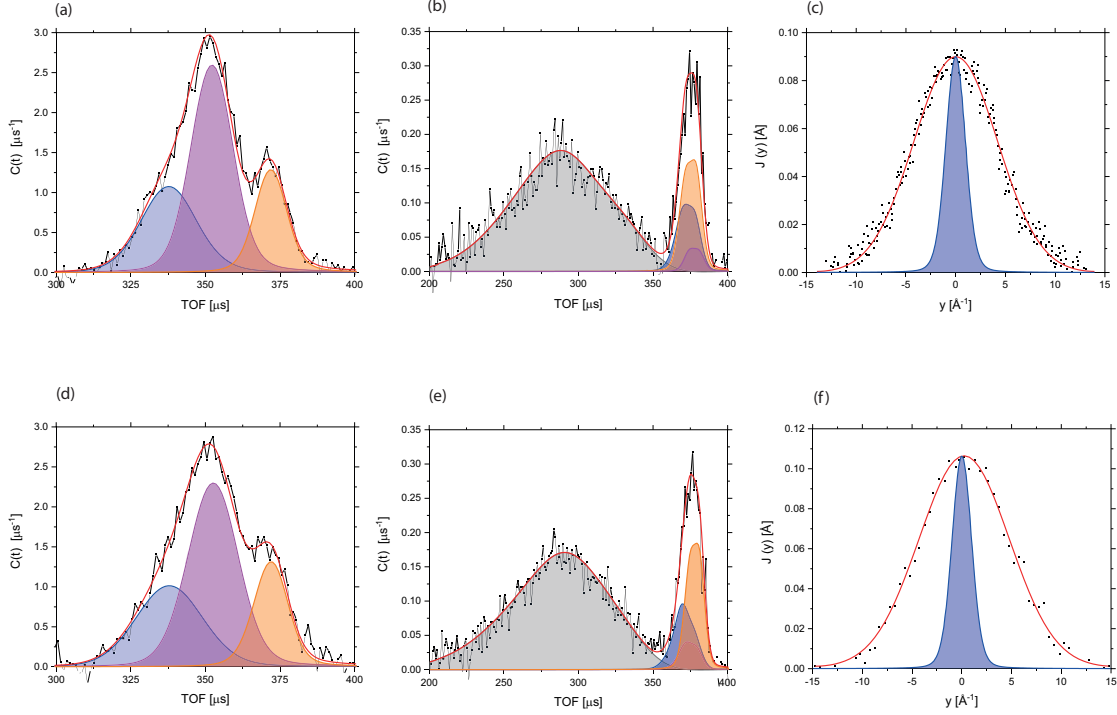
Figure 5: Mass-selective NCS spectra of a $WO_3 \cdot H_2O$, collected at T = 10 K (panels a, b, and c) and at T=300 K (panels d, e, and f) on the VESUVIO spectrometer (ISIS, STFC, UK). The black points refer to the experimental data, summed over all backward (panels a and d) and forward (panels b and e) detectors, respectively. The red lines indicate the fit of the summed data. The filled areas in panels a, b, d, and e, show, summed over respective detectors, fits to the recoil peaks of individual atomic species: hydrogen (in grey), oxygen (in blue), aluminium (in magenta), and tungsten (in orange). Panels c and f show the recoil peak data for the hydrogen transformed into the longitudinal momentum space of the hydrogen and fitted with underlying Gaussian momentum distribution functions. The areas filled in blue, shown in panels c and f, represent the hydrogen resolution function in its longitudinal momentum space.

in the system, which starts showing up in the nuclear dynamics of the protons above 100 K.

In order to put the deficit of the NMD widths, and in consequence, the anomalously low, compared to the *ab initio* LD and BOMD predictions, values of the nuclear kinetic energy of the protons in $WO_3 \cdot H_2O$, into perspective, in the top panel of Figure 6, values of NMD widths of protons in different water systems are compared with the values obtained from NCS experiments performed in this work. Clearly, the discrepancy seen in the region of temperature between T= 10K and T= 100K in $WO_3 \cdot H_2O$ is very similar to the deficit of NMD widths of the protons in single-wall carbon nanotubes (SWNT). Also, in the limit of

the room temperature, the values of NMD widths of the protons in $WO_3 \cdot H_2O$ are closer to the values obtained for liquid water and ice than to the values obtained for water protons in SWNT.[8,10]
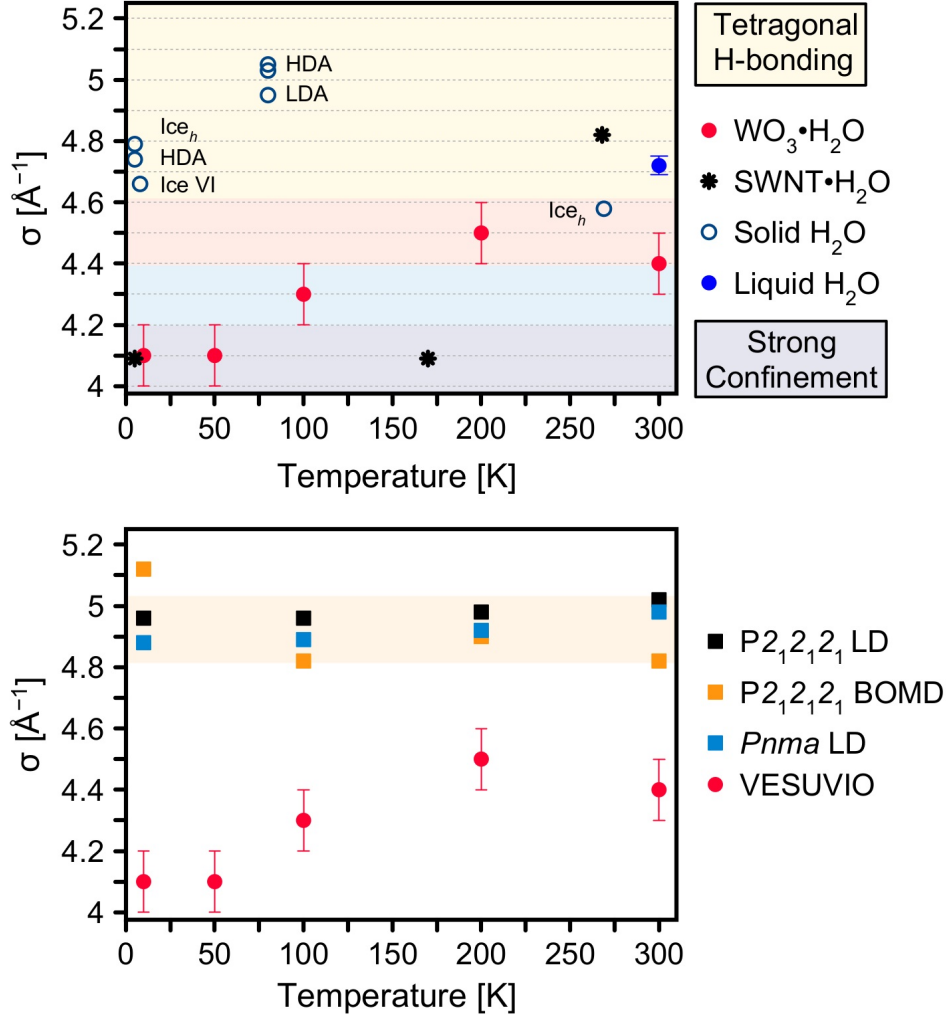

Figure 6: Upper panel: a comparison of the NMD widths of the protons in $WO_3 \cdot H_2O$ with the NCS results obtained in other systems where water is present.[10,32] Lower panel: The benchmarking of the NMD widths of the protons in $WO_3 \cdot H_2O$ against the predictions obtained from *ab initio* LD and BOMD simulations.

Water protons in $WO_3 \cdot H_2O$ below 100K seem to behave similarly to protons in structural water present in confined spaces of different materials.[8,10,14–17] Quasi-one-dimensional water and ice encapsulated inside single-walled carbon nanotubes was first studied ND and INS, augmented by MD simulations.[8] The 'shell-chain' structure of nanotube water obtained in

MD simulations, consistent with the results of the ND and INS experiments, could be summarised as consisting of two types of water, most of which were 'shell water molecules' frozen along the interior of the nanotube wall in a fourfold coordinated 'square-ice' pattern, and the remainder consisting of interior 'chain' water molecules.[8] The analysis of the vibrational densities of states of the nanotube ice as contrasted with its counterpart in the hexagonal ice revealed distinct features reflecting the soft hydrogen bond dynamics unique to nanotube ice that could be summarised as the overall softening of modes and shifting of the centre-of-gravity of the distribution of vibrations towards lower energies.[8] Taking into account that the nuclear kinetic energy can be expressed as the first moment of the Boltzmann-population weighted atom-projected vibrational densities of states,[19,22,23] this picture is consistent with lowering of the nuclear kinetic energy of protons in SWNT as compared to the hexagonal ice, and consistent with the lowering of the values of NMD widths of water protons in $WO_3 \cdot H_2O$ below 100K compared to the values of NMD widths of liquid water and ice observed in this work.

As the proton momentum distributions for systems at the zero-temperature limit are exclusively determined by proton wave functions being the ground state solutions of the nuclear Schroedinger equation, by virtue of the Heisenberg uncertainty principle, the narrowing of the NMD widths is inextricably intertwined with the concomitant broadening of the position distributions (i. e., spatial delocalisation) of the protons.[19,22,23] Beyond the zero-temperature limit, a version of the uncertainty principle exists based on the density matrix formulation, which boils down to expressing the variance of the position distribution of a nucleus through the minus first moment of the Boltzmann-population weighted atom-projected vibrational density of states.[19,22,23] Thus, at any temperature, the amount of spatial delocalisation of a nucleus is inversely proportional to its NMD width. This picture is consistent with the observation about water protons in SWNT, whose magnitude of the variance of the position distribution is about four times larger than that for hexagonal throughout the 8–273 K temperature range.[8] Taking into account the fact that the NMD widths of the water protons

in SWNT and in $WO_3 \cdot H_2O$ behave similarly below 100K, one can conclude that protons in $WO_3 \cdot H_2O$ are spatially delocalised with the magnitude of the variance of the position distribution of the order of four times that in liquid water.

The confinement-induced nuclear quantum delocalisation of protons can be dictated by different types of topology and interactions between water molecules and their surrounding. For water protons in SWNT, it is the confinement and the interaction with carbon nanotube walls, where the unique quantum state, qualitatively different from that of protons in the other phases of ice, is associated with the 2D ice sheath, where protons in the hydrogen bonds are coherently delocalised.[8,10] The peculiar behaviour of nuclear wave functions of the water protons induced by confinement is not necessarily reserved to composite systems where water is present in the form of guest molecules. It was found, by means of NCS, that some of the protons in water when it is doped with small amounts of acid or base are in fact incoherent bimodal distributions, indicating that the distribution of protons surrounding the impurity sites is strongly affected by their presence.[9] Finally, for water protons in $WO_3 \cdot H_2O$, it seems to be the interaction of a quasi-two-dimensional layer of structural water with the WO_6 octahedra that induces the highly quantum-coherent and spatially delocalised state of protons within the network of hydrogen bonds.

Apart from the observation of the nuclear quantum delocalisation of structural water protons and their concomitant anomalously low amount of kinetic energy, there is also a question of whether these water protons can exhibit nuclear quantum tunnelling. A new 'quantum tunnelling state' of the water molecule confined in 5 Å channels in the mineral beryl, characterised by extended proton and electron delocalisation, was evidenced by NCS.[14] In this state, water in the channels in the beryl structure tunnels between the six symmetrically equivalent positions around the c-axis, having an anomalously small proton kinetic energy due to spatial delocalisation. The observed tunnelling state of water in beryl is rather unusual compared to other known examples of rotational tunnelling of molecules, e.g., methyl and ammonia groups, where the tunnelling and localised (non-tunnelling) molecules look

unchanged.[14]

Interestingly, there is a visible effect of fine-tuning the confining geometry on the nuclear quantum dynamics of structural water, including its ability to exhibit nuclear quantum tunnelling. X-ray and neutron Compton scattering measurements of the electron and proton momentum distribution in water confined in both single-walled and double-walled carbon nanotubes (SWNT and DWNT), as a function of temperature and confinement size, revealed that the nuclear quantum delocalised state of water protons is sensitive to both temperature and the size of confinement.[92] This anomalous state exists in water confined in single-walled carbon nanotubes (SWNTs) of nominal diameter at 14 Å and double-walled carbon nanotubes (DWNTs) of nominal diameter at 16 Å. However, a visible reduction was observed in the average momentum width of the protons in the SWNT from that of bulk water, and the increase of that width for the DWNT would imply a more delocalised proton in the SWNT than that in the DWNT.[92] Moreover, as evidenced by INS studies of water in the channels of beryl and cordierite,[17] very small differences in the size (about 5.1 and 5.5 Å in diameter, for beryl and cordierite, respectively) and structure of the pores (with the pores in cordierite being slightly elongated) and the orientation of the water molecule in these minerals result in changes in the potential of the water protons and drastic changes in the confined water dynamics, including vanishing of the tunnelling behaviour in cordierite. If we treat the space between the two adjacent layers of the WO_6 octahedra in tungstic acid as a space available for the confinement of water molecules, the distance between the tungsten atom of one octahedron and an oxygen atom of an adjacent octahedron in the $P2_12_12_1$ crystal structure of tungstic acid from our refinement yields 4.48 Å, a value lower than the pore size in beryl. Thus, with the sensitivity of the tunnelling state of structural water protons to the confining geometry reported in the literature, it is difficult to assess if the geometry of the tungstic acid supports the tunnelling states of protons. Also, the quality of proton NMDs, as obtained directly from NCS experiments on tungstic acid, does not allow for fitting any underlying nuclear momentum distributions beyond a simple Gaussian model, and thus the

only hint towards the coherent delocalised state of protons is contained within the single nuclear quantum observable, the NMD width.

We close our discussion with the remark that, in the case of oxygen and tungsten in $WO_3 \cdot H_2O$, the values of NMD widths simulated based on the *ab initio* LD approach are in good agreement with the values from NCS experiments, as depicted in Figure 7, where *ab initio* LD simulations for the $P2_12_12_1$ model is shown.
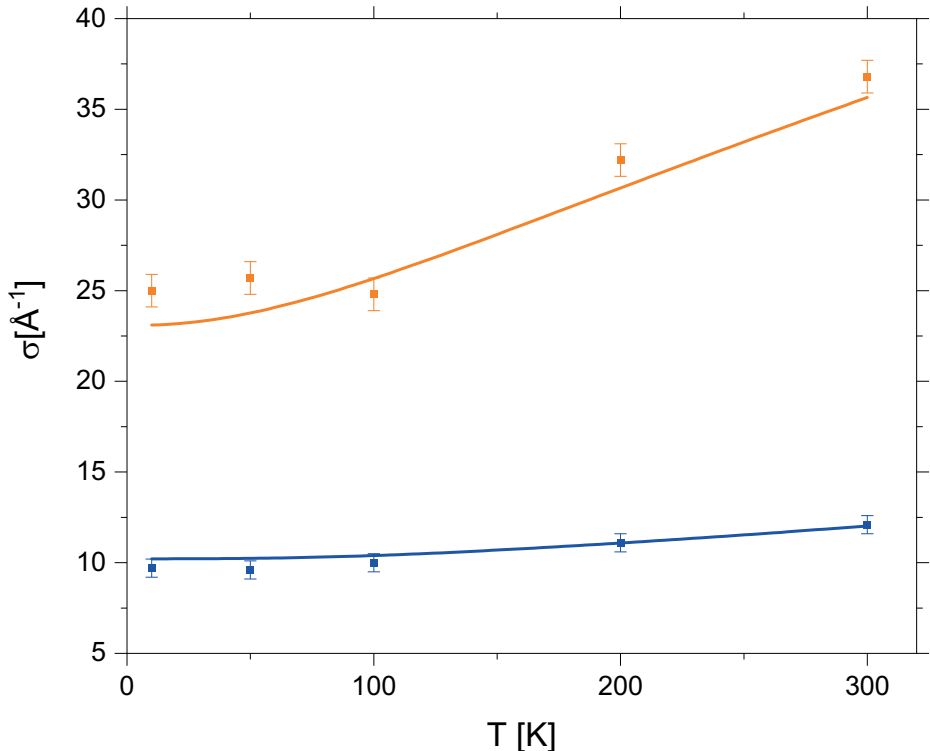

Figure 7: A comparison of the NMD widths of the oxygen (solid blue line) and tungsten (solid orange line) obtained from the *ab initio* LD simulations for tungstic acid with the values obtained from NCS experiments (blue and orange symbols, for oxygen and tungsten, respectively. See text for details.

On the whole, our results are a fully consistent with a quantum picture of protons, whereby the amount of nuclear quantum delocalisation, escaping the essentially classical character of *ab initio* LD and BOMD simulations, decreases with increasing temperature. Contrary to the protons, both oxygen and tungsten nuclei in $WO_3 \cdot H_2O$ can be satisfactorily

approximated as classical objects, even at cryogenic temperatures.

Conclusions

A global approach, consisting of concurrent application of ND, INS, NCS, and *ab initio* modelling, has been applied for the characterisation of the structure and local disorder-induced nuclear dynamics in the tungstic acid. The analysis of low-temperature powder ND data and INS spectra, augmented by harmonic phonon calculations, revealed that the *Pnma* structure of tungstic acid is not mechanically stable. Importantly, the rejection of the *Pnma* structure model immediately led to the conclusion that the structure of confined water is inconsistent with the picture whereby there are no interactions between the water molecules, which are solely H-bonded to the two neighbouring WO_3 polyhedra and perfectly aligned along the *ca* -mirror-plane. Instead, the analysis was shown to be more consistent with the $P2_12_12_1$ symmetry, characterised by a highly interconnected network of H-bonded water molecules confined in quasi-two-dimensional layers between the WO_3 polyhedra. Moreover, no structural phase transition was detected below room temperature, a feature consistent with the conclusion that water remains visibly confined in tungstic acid all across the range T = 1.5 – 300 K Despite the initial success of the *ab initio* harmonic LD calculations, the analysis has also shown a failure of the phonon calculations to fully account for the INS spectra due to the presence of a strongly anharmonic confining potential. Extending the computational route towards AIMD simulations allowed probing different structural configurations and provided an improved description of the vibrational dynamics as compared to high-resolution INS experiments. The AIMD simulations confirmed that the *Pnma* structure is not stable and immediately evolves toward the lowest-energy configuration described by the $P2_12_12_1$ symmetry, characterised by twisting of water molecules to satisfy interactions with the neighbours.

Owing to the mass-resolved nature of neutron Compton scattering, the appraisal of the

NQEs and the benchmarking of *ab initio* simulations could be performed separately for hydrogen, oxygen, and tungsten. The NMD widths of the oxygen and tungsten obtained from the *ab initio* harmonic LD simulations reproduce the experimental NCS results satisfactorily. This result, together with the fact that *ab initio* simulations assume a purely classical character of nuclei, leads to a conclusion that the manifestation of nuclear quantum effects in tungstic acid is limited to hydrogen.

In the case of hydrogen, the nuclear quantum character of the nucleus manifests itself clearly as a discrepancy between the *ab initio*-predicted values of NMD widths and their counterparts obtained from the experiments. The experimental NMD widths are ca. 20 per cent less than the theoretical predictions at temperatures below 100 K. With increasing temperature, the difference between the simulated and measured values decreases, but the theoretical predictions do not converge to experimental data, even at the limit of the room temperature. Fully accounting for the quantum character of protons in tungstic acid, especially at cryogenic temperatures, however, emerges as a challenge. To this end, one has to resort to fully quantum calculations within Path Integral Molecular Dynamics (PIMD) formalism, which, however, becomes prohibitively expensive due to the number of replicas required for convergence of calculated NMDs. In the future, applying deep neural network potentials[93] combined with accelerated PIMD calculations[94] can provide the means to address this challenge, and $WO_3 \cdot H_2O$ appears as an ideal candidate for a further benchmark of the state-of-the-art developments.

Taking into account that the amount of the deficit of the NMD widths of water protons $WO_3 \cdot H_2O$ obtained in this work is very similar to the one observed for protons in two-dimensional layers of highly confined and locally ordered water molecules present in carbon nanotubes and porous minerals, one can conclude that the confinement leads to nuclear quantum delocalisation of water protons in a highly correlated and locally ordered network of hydrogen bonds present in tungstic acid. As shown by previous NCS studies of structural water protons, in the presence of a fine-tuned confining geometry, the nuclear quantum

delocalisation of water protons can be accompanied by nuclear quantum tunnelling. The question if such behaviour is also present in the case of tungstic acid can only be answered by future NCS investigations on an upgraded NCS instrument, whose concept has already been proposed[19,23,55]

ASSOCIATED CONTENT

Acknowledgements

Supporting Information Available

This section includes benchmark of the theoretical calculations, additional computational results, and structural data for selected models. This material is available free of charge *via* the Internet at http://pubs.acs.org.

References

(1) Chen, Z.; Peng, Y.; Liu, F.; Le, Z.; Zhu, J.; Shen, G.; Zhang, D.; Wen, M.; Xiao, S.; Liu, C.-P.; et al., Hierarchical Nanostructured WO_3 with Biomimetic Proton Channels

and Mixed Ionic-Electronic Conductivity for Electrochemical Energy Storage. *Nano Lett.* **2015**, *15*, 6802–6808.

(2) Mitchell, J. B.; Lo, W. C.; Genc, A.; LeBeau, J.; Augustyn, V. Transition from Battery to Pseudocapacitor Behavior via Structural Water in Tungsten Oxide. *Chem. Mater.* **2017**, *29*, 3928–3937.

(3) Wang, R.; Mitchell, J. B.; Gao, Q.; Tsai, W.-Y.; Boyd, S.; Pharr, M.; Balke, N.; Augustyn, V. Operando Atomic Force Microscopy Reveals Mechanics of Structural Water Driven Battery-to-Pseudocapacitor Transition. *ACS Nano* **2018**, *12*, 6032–6039.

(4) Mitchell, J. B.; Geise, N. R.; Paterson, A. R.; Osti, N. C.; Sun, Y.; Fleischmann, S.; Zhang, R.; Madsen, L. A.; Toney, M. F.; Jiang, D.-e.; et al., Confined Interlayer Water Promotes Structural Stability for High-Rate Electrochemical Proton Intercalation in Tungsten Oxide Hydrates. *ACS Energy Lett.* **2019**, *4*, 2805–2812.

(5) Ceriotti, M.; Fang, W.; Kusalik, P. G.; McKenzie, R. H.; Michaelides, A.; Morales, M. A.; Markland, T. E. Nuclear Quantum Effects in Water and Aqueous Systems: Experiment, Theory, and Current Challenges. *Chem. Rev.* **2016**, *116*, 7529–7550.

(6) Markland, T. E.; Ceriotti, M. Nuclear Quantum Effects Enter the Mainstream. *Nat. Rev. Chem.* **2018**, *2*, 1–14.

(7) Reiter, G. F.; Mayers, J.; Platzman, P. Direct Observation of Tunneling in KDP using Neutron Compton Scattering. *Phys. Rev. Lett.* **2002**, *89*, 135505–4.

(8) Kolesnikov, A. I.; Zanotti, J.-M.; Loong, C.-K.; Thiyagarajan, P.; Moravsky, A. P.; Loutfy, R. O.; Burnham, C. J. Anomalously Soft Dynamics of Water in a Nanotube: A Revelation of Nanoscale Confinement. *Phys. Rev. Lett.* **2004**, *93*, 035503–4.

(9) Reiter, G.; Mayers, J.; Abdul-Redah, T. Coherence in the Momentum Distribution of Protons in Dilute Acids and Bases. *Physica B: Condens. Matter* **2006**, *385*, 234–235.

(10) Reiter, G.; Burnham, C.; Homouz, D.; Platzman, P. M.; Mayers, J.; Abdul-Redah, T.; Moravsky, A. P.; Li, J. C.; Loong, C. K.; Kolesnikov, A. I. Anomalous Behavior of Proton Zero Point Motion in Water Confined in Carbon Nanotubes. *Phys. Rev. Lett.* **2006**, *97*, 247801–4.

(11) Pantalei, C.; Pietropaolo, A.; Senesi, R.; Imberti, S.; Andreani, C.; Mayers, J.; Burnham, C.; Reiter, G. Proton Momentum Distribution of Liquid Water from Room Temperature to the Supercritical Phase. *Phys. Rev. Lett.* **2008**, *100*, 177801–4.

(12) Ceriotti, M.; Miceli, G.; Pietropaolo, A.; Colognesi, D.; Nale, A.; Catti, M.; Bernasconi, M.; Parrinello, M. Nuclear Quantum Effects in Ab Initio Dynamics: Theory and Experiments for Lithium Imide. *Phys. Rev. B* **2010**, *82,* 174306–5.

(13) Agapov, A. L.; Kolesnikov, A. I.; Novikov, V. N.; Richert, R.; Sokolov, A. P. Quantum Effects in the Dynamics of Deeply Supercooled Water. *Phys. Rev. E* **2015**, *91*, 022312–10.

(14) Kolesnikov, A. I.; Reiter, G. F.; Choudhury, N.; Prisk, T. R.; Mamontov, E.; Podlesnyak, A.; Ehlers, G.; Seel, A. G.; Wesolowski, D. J.; Anovitz, L. M. Quantum Tunneling of Water in Beryl: A New State of the Water Molecule. *Phys. Rev. Lett.* **2016**, *116*, 167802–6.

(15) Osti, N. C.; Naguib, M.; Ganeshan, K.; Shin, Y. K.; Ostadhossein, A.; van Duin, A. C. T.; Cheng, Y.; Daemen, L. L.; Gogotsi, Y.; Mamontov, E.; et al., Influence of Metal Ions Intercalation on the Vibrational Dynamics of Water Confined Between MXene Layers. *Phys. Rev. Mater.* **2017**, *1*, 065406–8.

(16) Kolesnikov, A. I.; Reiter, G. F.; Prisk, T. R.; Krzystyniak, M.; Romanelli, G.;

Wesolowski, D. J.; Anovitz, L. M. Inelastic and Deep Inelastic Neutron Spectroscopy of Water Molecules under Ultra-confinement. *J. Phys. Conf. Ser.* **2018**, *1055*, 012002–11.

(17) Kolesnikov, A. I.; Anovitz, L. M.; Hawthorne, F. C.; Podlesnyak, A.; Schenter, G. K. Effect of Fine-tuning Pore Structures on the Dynamics of Confined Water. *J. Chem. Phys.* **2019**, *150*, 204706–8.

(18) Moid, M.; Finkelstein, Y.; Moreh, R.; Maiti, P. K. Microscopic Study of Proton Kinetic Energy Anomaly for Nanoconfined Water. *J. Phys. Chem. B* **2020**, *124*, 190–198.

(19) Andreani, C.; Senesi, R.; Krzystyniak, M.; Romanelli, G.; Fernandez-Alonso, F. In *Neutron Scattering - Applications in Biology, Chemistry, and Materials Science*; Fernandez-Alonso, F., Price, D. L., Eds.; Experimental Methods in the Physical Sciences; Academic Press, 2017; Vol. 49; pp 403–457.

(20) Mayers, J.; Reiter, G. The VESUVIO Electron Volt Neutron Spectrometer. *Meas. Sci. Technol.* **2012**, *23*, 045902–18.

(21) Bowden, Z.; Celli, M.; Cilloco, F.; Colognesi, D.; Newport, R.; Parker, S.; Ricci, F.; Rossi-Albertini, V.; Sacchetti, F.; Tomkinson, J.; et al., The TOSCA Incoherent Inelastic Neutron Spectrometer: Progress and Results. *Physica B Condens. Matter* **2000**, *276-278*, 98–99.

(22) Andreani, C.; Colognesi, D.; Mayers, J.; Reiter, G. F.; Senesi, R. Measurement of Momentum Distribution of Light Atoms and Molecules in Condensed Matter Systems using Inelastic Neutron Scattering. *Adv. Phys.* **2005**, *54*, 377–469.

(23) Andreani, C.; Krzystyniak, M.; Romanelli, G.; Senesi, R.; Fernandez-Alonso, F. Electron-volt Neutron Spectroscopy: beyond Fundamental Systems. *Adv. Phys.* **2017**, *66*, 1–73.

(24) Ceriotti, M.; Manolopoulos, D. E. Efficient First-principles Calculation of the Quantum Kinetic Energy and Momentum Distribution of Nuclei. *Phys. Rev. Lett.* **2012**, *109*, 100604–5.

(25) Watson, G. I. Neutron Compton Scattering. *J. Phys.: Condens. Matter* **1996**, *8*, 5955–5975.

(26) Mayers, J. Measurement of the Proton Wave Function in Molecular Hydrogen by Neutron Compton Scattering. *Phys. Rev. Lett.* **1993**, *71*, 1553–1556.

(27) Homouz, D.; Reiter, G.; Eckert, J.; Mayers, J.; Blinc, R. Measurement of the 3D Born-Oppenheimer Potential of a Proton in a Hydrogen-Bonded System via Deep Inelastic Neutron Scattering: The Superprotonic Conductor $Rb_3H(SO_4)_2$. *Phys. Rev. Lett.* **2007**, *98*, 115502–4.

(28) Garbuio, V.; Andreani, C.; Imberti, S.; Pietropaolo, A.; Reiter, G. F.; Senesi, R.; Ricci, M. A. Proton Quantum Coherence Observed in Water Confined in Silica Nanopores. *J. Chem. Phys.* **2007**, *127*, 154501–10.

(29) M. Krzystyniak, M.; Abdul-Redah, T. Proton Momentum Distribution in Solid and Liquid HF. *Phys. Rev. B* **2010**, *82*, 064301–9.

(30) Krzystyniak, M.; Adams, M. A.; Lovell, A.; Skipper, N. T.; Bennington, S. M.; Mayers, J.; Fernandez-Alonso, F. Probing the Binding and Spatial Arrangement of Molecular Hydrogen in Porous Hosts via Neutron Compton Scattering. *Faraday Discuss.* **2011**, *151*, 171–197.

(31) Krzystyniak, M.; Fernandez-Alonso, F. Ab initio Nuclear Momentum Distributions in Lithium Hydride: Assessing Nonadiabatic Effects. *Phys. Rev. B* **2011**, *83*, 134305–10.

(32) Parmentier, A.; Shephard, J. J.; Romanelli, G.; Senesi, R.; Salzmann, C. G.; An-

dreani, C. Evolution of Hydrogen Dynamics in Amorphous Ice with Density. *J. Phys. Chem. Lett.* **2015**, *6*, 2038–2042.

(33) Romanelli, G.; Senesi, R.; Zhang, X.; Loh, K. P.; Andreani, C. Probing the Effects of 2D Confinement on Hydrogen Dynamics in Water and Ice Adsorbed in Graphene Oxide Sponges. *Phys. Chem. Chem. Phys.* **2015**, *17*, 31680–31684.

(34) Romanelli, G.; Liscio, A.; Senesi, R.; Zamboni, R.; Treossi, E.; Liscio, F.; Giambastiani, G.; Palermo, V.; Fernandez-Alonso, F.; Andreani, C. Soft Confinement of Water in Graphene-oxide Membranes. *Carbon* **2016**, *108*, 199–203.

(35) Andreani, C.; Romanelli, G.; Senesi, R. Direct Measurements of Quantum Kinetic Energy Tensor in Stable and Metastable Water near the Triple Point: An Experimental Benchmark. *J. Phys. Chem. Lett.* **2016**, *7*, 2216–2220.

(36) Cheng, B.; Behler, J.; Ceriotti, M. Nuclear Quantum Effects in Water at the Triple Point: Using Theory as a Link Between Experiments. *J. Phys. Chem. Lett.* **2016**, *7*, 2210–2215.

(37) Krzystyniak, M.; Drużbicki, K.; Romanelli, G.; Gutmann, M. J.; Rudić, S.; Imberti, S.; Fernandez-Alonso, F. Nuclear Dynamics and Phase Polymorphism in Solid Formic Acid. *Phys. Chem. Chem. Phys.* **2017**, *19*, 9064–9074.

(38) Fjellvåg, Ø. S.; Krzystyniak, M.; Vajeeston, P.; Sjåstad, A. O.; Armstrong, J. A Combined Deep Inelastic Neutron Scattering and Ab Initio Lattice Dynamics Study of the Hydride Anion Dynamics and Bonding in La_2LiHO_3 Oxyhydride. *J. Phys. Commun.* **2019**, *3*, 103002–7.

(39) Ulpiani, P.; Romanelli, G.; Onorati, D.; Krzystyniak, M.; Andreani, C.; Senesi, R. The Effective Isotropy of the Hydrogen Local Potential in Biphenyl and other Hydrocarbons. *J. Chem. Phys.* **2020**, *153*, 234306–11.

(40) Andreani, C.; Romanelli, G.; Parmentier, A.; Senesi, R.; Kolesnikov, A., I; Ko, H.-Y.; Andrade, M. F. C.; Car, R. Hydrogen Dynamics in Supercritical Water Probed by Neutron Scattering and Computer Simulations. *J. Phys. Chem. Lett.* **2020**, *11*, 9461–9467.

(41) Bocedi, A.; Romanelli, G.; Andreani, C.; Senesi, R. Hydrogen Nuclear Mean Kinetic Energy in Water Down the Mariana Trench: Competition of Pressure and Salinity. *J. Chem. Phys.* **2020**, *153*, 134306–6.

(42) Arnold, O.; Bilheux, J. C.; Borreguero, J. M.; Buts, A.; Campbell, S. I.; Chapon, L.; Doucet, M.; Draper, N.; Ferraz Leal, R.; Gigg, M. A.; *et al.*, Mantid - Data Analysis and Visualization Package for Neutron Scattering and μSR Experiments. *Nucl. Instrum. Methods Phys. Res. A* **2014**, *764*, 156–166.

(43) Chapon, L. C.; Manuel, P.; Radaelli, P. G.; Benson, C.; Perrott, L.; Ansell, S.; Rhodes, N. J.; Raspino, D.; Duxbury, D.; Spill, E.; et al., Wish: The New Powder and Single Crystal Magnetic Diffractometer on the Second Target Station. *Neutron News* **2011**, *22*, 22–25.

(44) Petrícek, V.; Dušek, M.; Palatinus, L. Crystallographic Computing System JANA2006: General features. *Z. Kristallogr.* **2014**, *229*, 345–352.

(45) Liebschner, D.; Afonine, P. V.; Urzhumtsev, A. G.; Adams, P. D. In *Neutron Crystallography in Structural Biology*; Moody, P. C., Ed.; Methods in Enzymology; Academic Press, 2020; Vol. 634; pp 177–199.

(46) Parker, S. F.; Fernandez-Alonso, F.; Ramirez-Cuesta, A. J.; Tomkinson, J.; Rudić, S.; Pinna, R. S.; Gorini, G.; Castañon, J. F. Recent and Future Developments on TOSCA at ISIS. *J. Phys. Conf. Ser.* **2014**, *554*, 012003–9.

(47) Pinna, R. S.; Rudić, S.; Capstick, M. J.; McPhail, D. J.; Pooley, D. E.; Howells, G. D.; Gorini, G.; Fernandez-Alonso, F. Detailed Characterisation of the Incident Neutron

Beam on the TOSCA Spectrometer. *Nucl. Instrum. Methods Phys. Res. A* **2017**, *870*, 79–83.

(48) Pinna, R. S.; Rudić, S.; Parker, S. F.; Armstrong, J.; Zanetti, M.; Škoro, G.; Waller, S. P.; Zacek, D.; Smith, C. A.; Capstick, M. J.; *et al.*, The Neutron Guide Upgrade of the TOSCA Spectrometer. *Nucl. Instrum. Methods Phys. Res. A* **2018**, *896*, 68–74.

(49) Pinna, R. S.; Zanetti, M.; Rudić, S.; Parker, S.; Armstrong, J.; Waller, S.; Zacek, D.; Smith, C.; Harrison, S.; Gorini, G.; et al., The TOSCA Spectrometer at ISIS: the Guide Upgrade and Beyond. *J. Phys. Conf. Ser.* **2018**, *1021*, 012029–4.

(50) Zanetti, M.; Bellissima, S.; del Rosso, L.; Masi, F.; Chowdhury, M.; Bonis, A. D.; Fresco, L. D.; Scatigno, C.; Armstrong, J.; Rudić, S.; *et al.*, Neutronic Developments on TOSCA and VESPA: Progress to Date. *Physica B Condens. Matter.* **2019**, *562*, 107–111.

(51) Krzystyniak, M.; Seel, A. G.; Richards, S. E.; Gutmann, M. J.; Fernandez-Alonso, F. Mass-selective Neutron Spectroscopy Beyond the Proton. *J. Phys. Conf. Ser.* **2014**, *571*, 012002–11.

(52) Ceriotti, M.; Drechsel-Grau, C.; Fernandez-Alonso, F.; Greaves, N.; Krzystyniak, M.; Major, D.; Parmentier, A.; Salzmann, C.; Senesi, R.; Sturniolo, S.; et al., Discussion: Theoretical Horizons and Calculation. *J. Phys. Conf. Ser.* **2014**, *571*, 012013–3.

(53) Andreani, C.; Ceriotti, M.; Chass, G.; Drechsel-Grau, C.; Fernandez-Alonso, F.; Greaves, N.; Gidopolous, N.; Krzystyniak, M.; Parmentier, A.; Refson, K.; et al., Discussion: Nuclear Quantum Dynamics - Protons and Beyond. *J. Phys. Conf. Ser.* **2014**, *571*, 012004–4.

(54) Palomino, L. R.; Dawidowski, J.; Helman, C.; Damián, J. M.; Romanelli, G.; Krzystyniak, M.; Rudić, S.; Cuello, G. Determination of the Scattering Cross Section of Calcium

using the VESUVIO Spectrometer. *Nucl. Instrum. Methods Phys. Res. A* **2019**, *927*, 443–450.

(55) Krzystyniak, M.; Romanelli, G.; Fabian, M.; Gutmann, M.; Festa, G.; Arcidiacono, L.; Gigg, M.; Drużbicki, K.; Andreani, C.; Senesi, R.; et al., VESUVIO plus: The Current Testbed for a Next-generation Epithermal Neutron Spectrometer. *J. Phys. Conf. Ser.* **2018**, *1021*, 012026–4.

(56) Romanelli, G.; Krzystyniak, M.; Senesi, R.; Raspino, D.; Boxall, J.; Pooley, D.; Moorby, S.; Schooneveld, E.; Rhodes, N. J.; Andreani, C.; et al., Characterisation of the Incident Beam and Current Diffraction Capabilities on the VESUVIO Spectrometer. *Meas. Sci. Technol.* **2017**, *28*, 095501–6.

(57) Seel, A. G.; Krzystyniak, M.; Fernandez-Alonso, F. The VESUVIO Spectrometer Now and When? *J. Phys. Conf. Ser.* **2014**, *571*, 012006–11.

(58) Jackson, S.; Krzystyniak, M.; Seel, A. G.; Gigg, M.; Richards, S. E.; Fernandez-Alonso, F. VESUVIO Data Analysis Goes MANTID. *J. Phys. Conf. Ser.* **2014**, *571*, 012009–18.

(59) Andreani, C.; Ceriotti, M.; Fernandez-Alonso, F.; Gorini, G.; Krzystyniak, M.; Parmentier, A.; Parker, S.; Seel, A.; Senesi, R.; Walewski, L. Discussion: Measurement and Instrumentation. *J. Phys. Conf. Ser.* **2014**, *571*, 012010–2.

(60) Krzystyniak, M.; Drużbicki, K.; Fernandez-Alonso, F. Nuclear Dynamics in the Metastable Phase of the Solid Acid Caesium Hydrogen Sulfate. *Phys. Chem. Chem. Phys.* **2015**, *17*, 31287–31296.

(61) Wallis, J.; Kruth, A.; da Silva, I.; Krzystyniak, M. Nuclear dynamics in $BaZr_{0.7}Ce_{0.2}Y_{0.1}O_3$-$\delta$ Proton Conductor as Observed by Neutron Diffraction and Compton Scattering. *J. Phys. Commun.* **2020**, *4*, 045004–21.

(62) Szymanski, J. T.; Roberts, A. C. The Crystal Structure of Tungstite, $WO_3.H_2O$. *Can. Mineral.* **1984**, *22*, 681–688.

(63) Payne, M. C.; Teter, M. P.; Allan, D. C.; Arias, T.; Joannopoulos, J. D. Iterative Minimization Techniques for Ab Initio Total-energy Calculations - Molecular-Dynamics and Conjugate Gradients. *Rev. Mod. Phys.* **1992**, *64*, 1045–1097.

(64) Clark, S. J.; Segall, M. D.; Pickard, C. J.; Hasnip, P. J.; Probert, M. I. J.; Refson, K.; Payne, M. C. First Principles Methods Using CASTEP. *Z. Kristallogr.* **2005**, *220*, 567–570.

(65) Hutter, J.; Iannuzzi, M.; Schiffmann, F.; VandeVondele, J. CP2K: Atomistic Simulations of Condensed Matter Systems. *Wiley Interdiscip. Rev. Comput. Mol. Sci.* **2013**, *4*, 15–25.

(66) VandeVondele, J.; Krack, M.; Mohamed, F.; Parrinello, M.; Chassaing, T.; Hutter, J. Quickstep: Fast and Accurate Density Functional Calculations using a Mixed Gaussian and Plane Waves Approach. *Comput. Phys. Commun.* **2005**, *167*, 103–128.

(67) Dovesi, R.; Erba, A.; Orlando, R.; Zicovich-Wilson, C. M.; Civalleri, B.; Maschio, L.; Rérat, M.; Casassa, S.; Baima, J.; Salustro, S.; et al., Quantum-mechanical Condensed Matter Simulations with CRYSTAL. *Wiley Interdiscip. Rev. Comput. Mol. Sci.* **2018**, *8*, e1360.

(68) McNellis, E.; Meyer, J.; Reuter, K. Azobenzene at Coinage Metal Surfaces: Role of Dispersive van der Waals Interactions. *Phys. Rev. B* **2009**, *80*, 205414–10.

(69) Baroni, S.; Giannozzi, P.; Testa, A. Green's-function Approach to Linear Response in Solids. *Phys. Rev. Lett.* **1987**, *58*, 1861–1864.

(70) Gonze, X. Perturbation Expansion of Variational Principles at Arbitrary Order. *Phys. Rev. A* **1995**, *52*, 1086–1095.

(71) Gonze, X. Adiabatic Density-Functional Perturbation Theory. *Phys. Rev. A* **1995**, *52*, 1096–1114.

(72) Dymkowski, K.; Parker, S. F.; Fernandez-Alonso, F.; Mukhopadhyay, S. AbINS: The Modern Software for INS Interpretation. *Physica B Condens. Matter* **2018**, *551*, 443–448.

(73) Cheng, Y. Q.; Daemen, L. L.; Kolesnikov, A. I.; Ramirez-Cuesta, A. J. Simulation of Inelastic Neutron Scattering Spectra Using OCLIMAX. *J. Chem. Theory Comput.* **2019**, *15*, 1974–1982.

(74) Perdew, J. P.; Burke, K.; Ernzerhof, M. Generalized Gradient Approximation Made Simple. *Phys. Rev. Lett.* **1996**, *77*, 3865–3868.

(75) Grimme, S.; Antony, J.; Ehrlich, S.; Krieg, H. A Consistent and Accurate Ab Initio Parametrization of Density Functional Dispersion Correction (DFT-D) for the 94 Elements H-Pu. *J. Chem. Phys.* **2010**, *132*, 154104–19.

(76) Grimme, S.; Ehrlich, S.; Goerigk, L. Effect of the Damping Function in Dispersion Corrected Density Functional Theory. *J. Comput. Chem.* **2011**, *32*, 1456–1465.

(77) Becke, A. D.; Johnson, E. R. A Density-functional Model of the Dispersion Interaction. *J. Chem. Phys.* **2005**, *123*, 154101–9.

(78) Drużbicki, K.; Krzystyniak, M.; Hollas, D.; Kapil, V.; Slavíček, P.; Romanelli, G.; Fernandez-Alonso, F. Hydrogen Dynamics in Solid Formic Acid: Insights from Simulations with Quantum Colored-noise Thermostats. *J. Phys. Conf. Ser.* **2018**, *1055*, 012003.

(79) Drużbicki, K.; Lavén, R.; Armstrong, J.; Malavasi, L.; Fernandez-Alonso, F.; Karlsson, M. Cation Dynamics and Structural Stabilization in Formamidinium Lead Iodide Perovskites. *J. Phys. Chem. Lett.* **2021**, *12*, 3503–3508.

(80) Ceriotti, M.; Manolopoulos, D. E.; Parrinello, M. Accelerating the Convergence of Path Integral Dynamics with a Generalized Langevin Equation. *J. Chem. Phys.* **2011**, *134*, 084104–9.

(81) Ceriotti, M.; Parrinello, M.; Markland, T. E.; Manolopoulos, D. E. Efficient Stochastic Thermostatting of Path Integral Molecular Dynamics. *J. Chem. Phys.* **2010**, *133*, 124104–13.

(82) Brehm, M.; Kirchner, B. TRAVIS - A Free Analyzer and Visualizer for Monte Carlo and Molecular Dynamics Trajectories. *J. Chem. Inf. Model.* **2011**, *51*, 2007–2023.

(83) Thomas, M.; Brehm, M.; Fligg, R.; Vöhringer, P.; Kirchner, B. Computing Vibrational Spectra from *Ab Initio* Molecular Dynamics. *Phys. Chem. Chem. Phys.* **2013**, *15*, 6608–6622.

(84) Cheng, Y. Q.; Kolesnikov, A. I.; Ramirez-Cuesta, A. J. Simulation of Inelastic Neutron Scattering Spectra Directly from Molecular Dynamics Trajectories. *J. Chem. Theory Comput.* **2020**, *16*, 7702–7708.

(85) Krzystyniak, M.; Richards, S. E.; Seel, A. G.; Fernandez-Alonso, F. Mass-selective Neutron Spectroscopy of Lithium Hydride and Deuteride: Experimental Assessment of the Harmonic and Impulse Approximations. *Phys. Rev. B* **2013**, *88*, 184304–16.

(86) Daniel, M.; Desbat, B.; Lassegues, J.; Gerand, B.; Figlarz, M. Infrared and Raman study of WO_3 Tungsten Trioxides and WO_3, xH_2O Tungsten Trioxide Hydrates. *J. Solid State Chem.* **1987**, *67*, 235–247.

(87) Chen, L.; Mashimo, T.; Okudera, H.; Iwamoto, C.; Omurzak, E. Synthesis of WO_3·H2O Nanoparticles by Pulsed Plasma in Liquid. *RSC Adv.* **2014**, *4*, 28673–28677.

(88) Williams, R. W.; Heilweil, E. J. Measuring Molecular Force Fields: Terahertz, Inelastic

Neutron Scattering, Raman, FTIR, DFT, and BOMD Molecular Dynamics of Solid L-serine. *Chem. Phys.* **2010**, *373*, 251–260.

(89) Williams, R. W.; Schlücker, S.; Hudson, B. S. Inelastic Neutron Scattering, Raman, Vibrational Analysis with Anharmonic Corrections, and Scaled Quantum Mechanical Force Field for Polycrystalline L-alanine. *Chem. Phys.* **2008**, *343*, 1–18.

(90) Parker, S. F.; Ramirez-Cuesta, A. J.; Albers, P. W.; Lennon, D. The Use of Direct Geometry Spectrometers in Molecular Spectroscopy. *J. Phys. Conf. Ser.* **2014**, *554*, 012004–9.

(91) Brieuc, F.; Bronstein, Y.; Dammak, H.; Depondt, P.; Finocchi, F.; Hayoun, M. Zero-Point Energy Leakage in Quantum Thermal Bath Molecular Dynamics Simulations. *J. Chem. Theory Comput.* **2016**, *12*, 5688–5697.

(92) Reiter, G. F.; Deb, A.; Sakurai, Y.; Itou, M.; Kolesnikov, A. I. Quantum Coherence and Temperature Dependence of the Anomalous State of Nanoconfined Water in Carbon Nanotubes. *J. Phys. Chem. Lett.* **2016**, *7*, 4433–4437.

(93) Zhang, C.; Tang, F.; Chen, M.; Xu, J.; Zhang, L.; Qiu, D. Y.; Perdew, J. P.; Klein, M. L.; Wu, X. Modeling Liquid Water by Climbing up Jacob's Ladder in Density Functional Theory Facilitated by Using Deep Neural Network Potentials. *The Journal of Physical Chemistry B* **0**, *0*, null, PMID: 34533960.

(94) Kapil, V.; Cuzzocrea, A.; Ceriotti, M. Anisotropy of the Proton Momentum Distribution in Water. *J. Phys. Chem. B* **2018**, *122*, 6048–6054.

Supplementary Information for Publication:

Interplay Between Local Structure and Nuclear Dynamics in Tungstic Acid: a Neutron Scattering Study

Erwin Lalik,[†] Kacper Drużbicki,[‡,¶] Gavin Irvine,[§] Matthias Gutmann,[∥] Svemir Rudić,[∥] Pascal Manuel,[∥] Václav Petříček,[⊥] and Matthew Krzystyniak[*,∥]

[†]Jerzy Haber Institute of Catalysis and Surface Chemistry, Polish Academy of Sciences, Niezapominajek 8, 30-239 Cracow, Poland

[‡]Materials Physics Center, CSIC-UPV/EHU, Paseo Manuel Lardizábal 5, 20018 Donostia-San Sebastian, Spain

[¶]Centre of Molecular and Macromolecular Studies, Polish Academy of Sciences, Sienkiewicza 112, 90-363 Lodz, Poland

[§]School of Chemistry, University of St Andrews, St Andrews, Fife KY16 9ST, United Kingdom

[∥]ISIS Facility, Rutherford Appleton Laboratory, Chilton, Didcot, OX11 0QX, United Kingdom

[⊥]Institute of Physics, Czech Academy of Sciences, Na Slovance 1999/2, Praha 8, 182 21, Czech Republic

E-mail: matthew.krzystyniak@stfc.ac.uk

Table S1: Cell constants (a, b, c) and lengths of non-equivalent W-O bonds in $WO_3 \cdot H_2O$ (*Pnma*) from experimental data (SXRD, PXRD – ambient conditions, RT; and NPD at 1.5 K with two alternative refinements) and theoretical calculations (CASTEP PW-DFT and CRYSTAL17 LCAO). Atom labelling according to Szymański *et al.* [*Can. Mineral.* **1984**, *22*, 681—688.]. All values are in Å. please note an improper W-O(1) and W-O(2) distances obtained with unconstrained refinement of the *Pnma* model (NPD-ALT).

Model	a	b	c	W-O(1)	W-O(2)	W-O(3)	W-O(5)
EXPERIMENTAL							
SXRD RT	5.2490	10.7110	5.1330	2.34	1.69	1.83	1.93
NPD	5.2424	10.6411	5.1550	2.27	1.86	1.84	1.95
NPD-ALT	5.2439	10.6542	5.1484	1.98	2.13	1.78	1.95
CASTEP PW-DFT							
LDA	5.3185	10.3495	5.0720	2.21	1.74	1.85	1.93
rPBE-TS	5.4282	10.5298	5.1198	2.27	1.75	1.83	2.05
PBEsol-TS	5.3409	10.5770	5.1342	2.25	1.74	1.86	1.94
PBE-MBD*	5.3556	10.7196	5.1511	2.31	1.74	1.88	1.94
PBE-TS	5.3735	10.8327	5.1668	2.32	1.74	1.87	1.95
PBE-D3(BJ)	5.3648	10.8497	5.1749	2.31	1.74	1.87	1.95
PBEsol	5.3283	11.2299	5.2142	2.26	1.74	1.86	1.94
PBE	5.3483	11.9905	5.3148	2.35	1.74	1.88	1.95
rPBE	5.3623	12.8435	5.3699	2.48	1.74	1.89	1.96
CRYSTAL17 LCAO							
PBE	5.4525	11.1855	5.2892	2.40	1.68	1.74	2.23
PBE0	5.3703	11.1041	5.1662	2.38	1.66	1.73	2.16
PBE-D3(BJ)	5.4017	10.7951	5.1150	2.39	1.68	1.74	2.19
PBE0-D3(BJ)	5.3390	10.6869	5.0220	2.35	1.66	1.73	2.14

Table S2: Comparison of the reliability factors obtained in the course of constrained refinement of the low-temperature neutron diffraction data (1.5 K) for the powder $WO_3 \cdot H_2O$ specimen versus two alternative structural models of tungstic acid considered in this work.

Reliability Factor	*Pnma*	*$P2_1 2_1 2_1$*
_refine_ls_R_factor_gt	0.0410	0.0596
_refine_ls_wR_factor_gt	0.0422	0.0396
_refine_ls_R_factor_all	0.0440	0.0657
_refine_ls_wR_factor_all	0.0424	0.0409
_refine_ls_goodness_of_fit_all	3.3719	2.8649

.

Table S3: Cell constants (*a*, *b*, *c*) and lengths of non-equivalent W-O bonds for the two alternative structural models of $WO_3 \cdot H_2O$ (*Pnma*). The experimental data (NPD at 1.5 K with two alternative refinements) versus theoretical predictions (CASTEP PW-DFT, PBE-TS) using both total-energy optimization at 0 K and low-temperature AIMD simulations. Atom labelling according to Szymański *et al.* [*Can. Mineral.* **1984**, *22*, 681—688.]. All values are in Å.

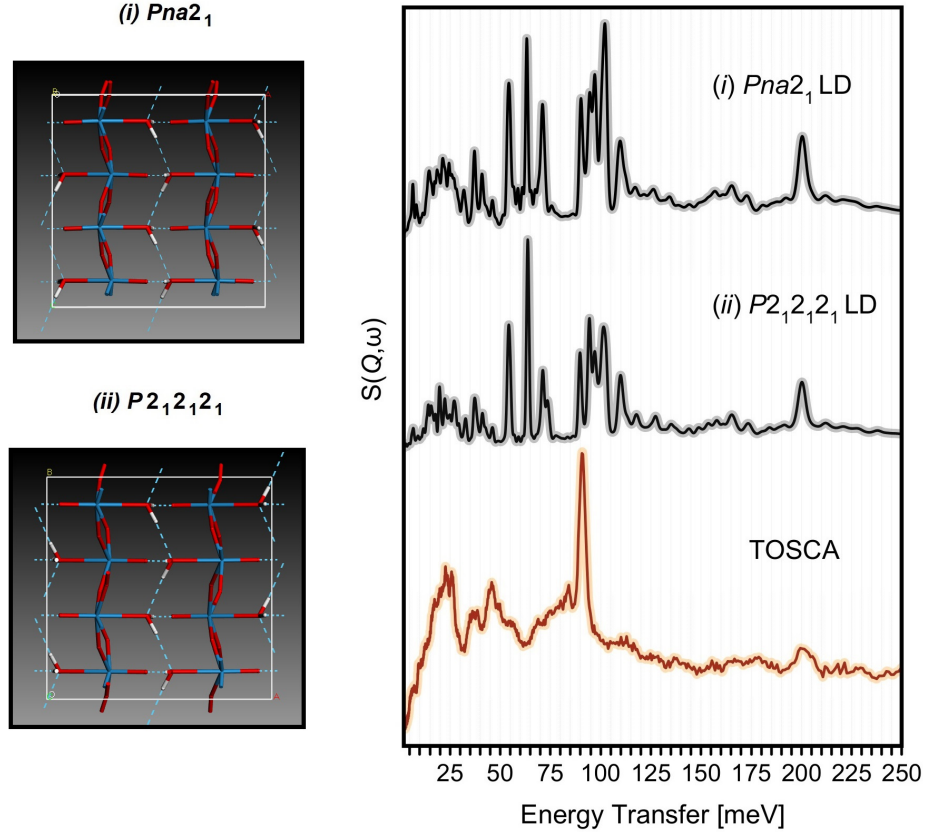| Model	*a*	*b*	*c*	W-O(1)	W-O(2)	W-O(3-4)	W-O(5-6)
NPD *Pnma* 1.5 K	5.2423	10.6410	5.1553	2.27	1.87	1.84	1.95
DFT-D *Pnma* 0 K	5.3735	10.8327	5.1668	2.32	1.74	1.87	1.95
DFT-D AIMD 10 K	5.3630	10.8115	5.1567	2.34	1.72	1.83	2.03
NPD $P2_12_12_1$ 1.5 K	10.6537	5.2486	5.1474	2.27	1.74	1.85 (av.)	1.92 (av.)
DFT-D $P2_12_12_1$ 0 K	10.6898	5.2799	5.2695	2.40	1.73	1.90 (av.)	1.93 (av.)
DFT-D AIMD 10 K	10.7126	5.3012	5.2792	2.40	1.74	1.85 (av.)	2.00 (av.)

Figure S1: Comparison of the experimental INS spectrum of $WO_3 \cdot H_2O$ (TOSCA at 10K) with the results of harmonic LD predictions performed for two nearly iso-energetic and fully mechanically-stable models (see the main text): [(i)] $Pna2_1$ and [(ii)] $P2_1P2_1P2_1$, respectively. Note slightly different distribution of spectral intensities for each model, while preserving the band positions. The cartoons shows the structure of both models under consideration in a 1×2×2 supercell projection.

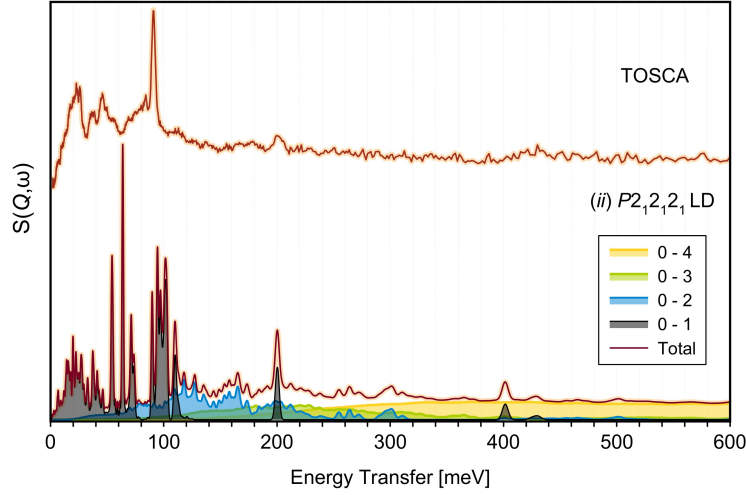Figure S2: Comparison of the experimental INS spectrum of $WO_3 \cdot H_2O$ (TOSCA at 10K presented in the range 0 – 600 meV) with the results of harmonic LD predictions performed for fully mechanically-stable model $^{(ii)}P2_1P2_1P2_1$. The theoretical INS spectrum (Total) has been decomposed into contributions from fundamentals, n = 1 (0–1) and higher-order transitions, n = 2 – 4 (0–2, 0–3, and 0–4). Note a vanishing contributions of n = 1 with increasing energy transfer and the opposite effect shown by n = 2 – 4.

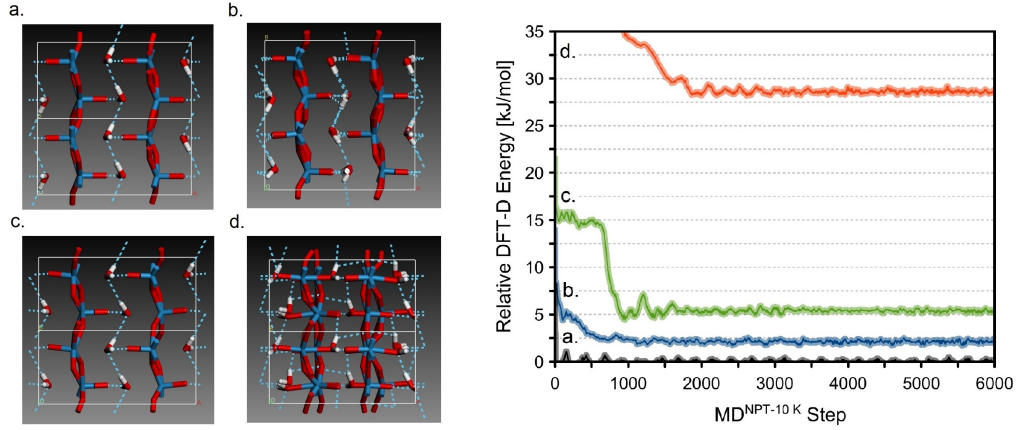Figure S3: Time evolution (1 fs / step) of the potential energy of $WO_3 \cdot H_2O$ (kJ/mol per formula unit) according to NPT-AIMD (plane-wave GGA-DFT-D) simulations at 10 K as referenced to the lowest-energy model. The simulations were performed on the $1 \times 2 \times 2$ supercell models without any symmetry constraints. The final snapshots are provided for each model considered in the cartoons, defined as follows: (a.) was initiated from the lowest-energy $^{(ii)}P2_1P2_1P2_1$ structure; (b.) was initiated with the *Pnma* model of the structure, which has trapped into a hydrogen-disordered configuration once evolving toward the lowest-energy (a.) configuration upon switching off the symmetry constraints; (c.) was based on the *Pnma*-alt structure, being non-preferable one in terms of energy and volume; (d.) is a massively-disordered structure, constructed by translating the water molecules in the interlayer space.
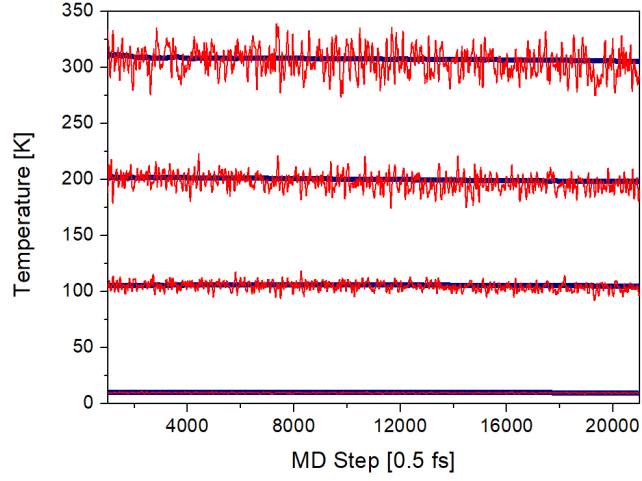
S4

Figure S4: Time evolution (0.5 fs / step) of the temperature (10, 100, 200, and 300 K) in the 10 ps long NVE-AIMD production run of the MD simulations relying on the $^{(ii)}P2_1P2_1P2_1$ model of the $WO_3 \cdot H_2O$ structure.

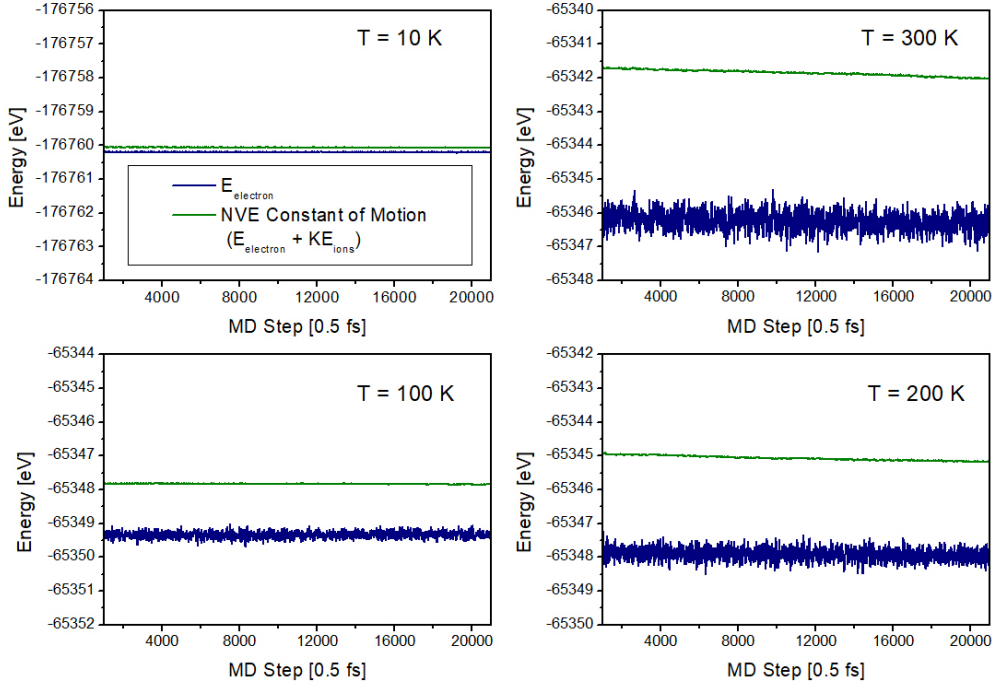

Figure S5: Time evolution (0.5 fs / step) of the potential energy ($E_{electron}$ and the constant of motion ($E_{electron} + KE_{ions}$) in the 10 ps long NVE-AIMD production runs (at 10, 100, 200, and 300 K) from the MD simulations relying on the $^{(ii)}P2_1P2_1P2_1$ model of the $WO_3 \cdot H_2O$ structure.